LATVIAN JOURNAL of PHYSICS and TECHNICAL SCIENCES

ISSN 0868 - 8257

3

Institue of Physical Energetics-70

(Vol. 53)

2016

Ind. pasūt. € 1,50 Indekss 2091
Org. € 15,00 Indekss 2092

SATURS

ENERĢĒTIKAS FIZIKĀLĀS UN TEHNISKĀS PROBLĒMAS

CIETVIELU FIZIKA

VIDES MONITORINGS

Price to individual subscribers € 1.50/issue Index 2091
Price to collective subscribers € 15.00/issue Index 2092

CONTENTS

PHYSICAL AND TECHNICAL ENERGY PROBLEMS

SOLID STATE PHYSICS

ENVIRONMENTAL MONITORING

Индивид. заказ. Є 1,50 Индекс 2091
Орг. заказ. Є 15,00 Индекс 2092

СОДЕРЖАНИЕ

LATVIAN JOURNAL of PHYSICS and TECHNICAL SCIENCES

LATVIJAS FIZIKAS un TEHNISKO ZINĀTŅU ŽURNĀLS

ЛАТВИЙСКИЙ ФИЗИКО-ТЕХНИЧЕСКИЙ ЖУРНАЛ

Published six times a year since February 1964
Iznāk sešas reizes gadā kopš 1964. gada februāra
Выходит шесть раз в год с февраля 1964 года

3 (Vol. 53) • 2016

RĪGA

INDEKSĒTS (PUBLICĒTS) | INDEXED (PUBLISHED) IN

www.scopus.com
www.degruyter.com
EBSCO (Academic Search Complete, www.epnet.com), INSPEC (www.iee.org.com).
VINITI (www.viniti.ru), Begell House Inc/ (EDC, www.edata-center.com).

Izdevējs: Fizikālās enerģētikas institūts
Reģistrācijas apliecība Nr. 0221
Redakcija: Aizkraukles ielā 21, Rīga, LV-1006
Tel. 67551732, 67558694
e-pasts: ezerniec@edi.lv
Interneta adrese: www.fei-web.lv
Iespiests SIA "AstroPrint"

LATVIAN JOURNAL OF PHYSICS AND TECHNICAL SCIENCES
2016, N 3

DOI: 10.1515/lpts-2016-0016

PHYSICAL AND TECHNICAL ENERGY PROBLEMS

INVESTIGATIONS OF WIND SHEAR DISTRIBUTION ON THE BALTIC SHORE OF LATVIA

V. Bezrukovs[1, 2], A. Zacepins[1], Vl. Bezrukovs[2], V. Komashilovs[1]

[1]Institute of Physical Energetics, 21 Aizkraukles Str.,
Riga, LV-1006, LATVIA
[2]Ventspils University College, 101 Inzenieru Str.,
Ventspils, LV-3601, LATVIA
e-mail: elmag@inbox.lv

The paper presents a review of wind parameter measurement complexes and investigation methods used for potential wind energy evaluation. Based on results of long-term investigations of wind shear distribution regularities are shown up to 160 m height on the Baltic Sea shore. Distribution of potential wind energy in Latvia is shown as a map and table of average and average cubic wind speed values. Database of wind parameter measurements is available at a public website.

Key words: *website, wind map, wind shear, wind speed measurement.*

1. INTRODUCTION

When designing wind power plants (WPPs), one of the main criteria for evaluating the commercial use of wind energy is availability of reliable information on the force of wind streams and their distribution in height. Investigations show that for the countries of the Baltic region it is typical that the wind turbines (WTs) work inefficiently at the height below 100 m [1]. The results of direct measurements of the wind speed for corresponding heights at the site of WPP construction are very valuable while estimating the expected recoupment terms for the relevant WPP developing projects.

Continuous perfection of the design for wind power generators is conducive to their operational efficiency, which means shorter recoupment terms for the costs of building the WPPs. Therefore, in Latvia under wide discussion there are the issues of attraction of investments – both at the state level and in the business environment – for WPP building.

2. METHODS OF WIND ENERGY FLOW INVESTIGATION

In most cases, for wind speed measurements the measuring sensors are employed whose mounting on a 50–60 m high mast is simple enough, or it is possible to use the masts for cellular communications [2], [3] disposed at a small distance from the WPP building site. Depending on landscape this distance should not exceed 2–4 km.

Wind energy potential evaluation on height of 24 m was performed using the Symphonie measurement complex during construction of the first WPP in Ainazi (Latvia) in 1994. This WPP consisted of two WTs with power of 600 kW [4]. Later on for wind shear investigations, mobile measurement sensors NRG #40 and NRG #200 were used for recording of wind speed and wind direction. Sensors were mounted on 50–60 m high masts in Ventspils district Irbene (site 1) and in Matishi (site 2) [1].

As a main recorder in the measurement system, LOGGER Symphonie 9200 is used, which performs recording of wind speed, wind direction and ambient temperature indicators with interval of 3 seconds. Afterwards the recorder performs averaging of obtained data for 10-min intervals and stores the results on the SD card, which can be used for further analysis. The unit is powered by two 1.5 V batteries, whose capacity is enough for 4–5 month of interruptible system operation.

Figures 1 – 5 demonstrate the registration unit LOGGER Symphonie 9200 and sensors for wind speed NRG #40 (S), wind direction NRG #200, temperature NRG #110s and air pressure NRG BR-20 measurements, which are mounted on metal mast at a height of 60 m.

Fig. 1. Registration unit LOGGER Symphonie 9200 for recoding data from sensors of wind speed NRG #40, vane NRG #200, temperature NRG #110s and air pressure NRG BR-20.

Fig. 2. Sensors for wind speed NRG #40, vane NRG #200, which are mounted on mast.

For wind energy estimation at a height up to 200 m optical remote sensing complexes with Light Detection and Ranging (LIDAR) technologies ZephIR and Pentalum SpiDAR were used.

Complex ZephIR (Fig. 6) was installed on the balcony of floor 8 of Ventspils College building (site 3) located 800 m from sea shore within the framework of FP7 project “NORSEWInD” [5].

Fig. 3. Temperature sensors NRG #110s.

Fig. 4. Air pressure sensor NRG BR-20.

Fig. 5. Installation of the 60-m high mast with a measuring complex Symphonie 9200 together with sensors on metal 1.8-m long mounting boom (site 2).

Fig. 6. Optical remote sensing complex ZephIR for measuring wind speed and direction at a distance up to height of 160 m on five height levels (located in Ventspils, site 3).

Figure 7 demonstrates laser measuring complex Pentalum SpiDAR, which was installed in the territory of Ventspils International Radio Astronomy Centre at the height of 13.2 m above ground level and at a distance of 2.5 km from the sea shore on a platform with coordinates N 57º33´12.00″ and E 21º51´16.00″ (site 4).

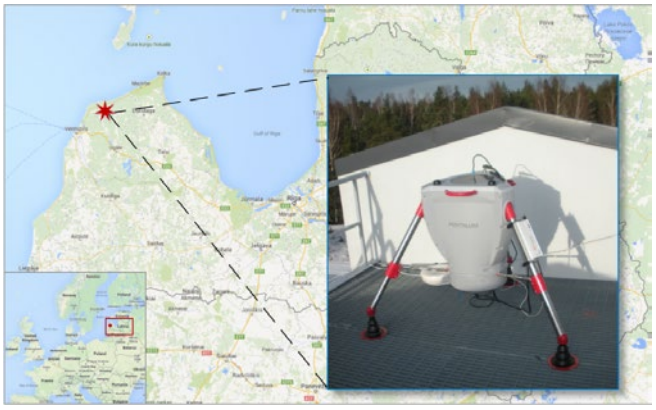

Fig. 7. Laser measuring complex Pentalum SpiDAR installed on the Baltic Sea shore at a height of 13.2 m above ground (site 4).

For the data transmission an optical communication line was employed which connects the measuring complex with server at Ventspils University College. The Pentalum SpiDAR performed 5 s measurements of wind speed and direction for ten height levels: 30, 40, 50, 80, 100, 120, 140, 160, 180 and 200 m. Apart from that, the records were made for pressure, humidity, and temperature of the air.

3. THE RESULTS OF WIND SHEAR INVESTIGATION

As a result of systematic, long-term measurements and evaluations of wind energy in Latvia, a huge amount of statistical data was collected for wind shear investigation on the Baltic Sea shore in Ventspils and Ainazi regions.

From the analysis of the statistical data reported in [5], [6], it follows that the curve of the average long-term wind speed distribution at height $V_{avg.h}$ is well approximated by the power law function:

$$V_{avg.h} = V_{avg.ref} \left(\frac{h}{h_{ref} - h_0}\right)^{\alpha}, \quad (1)$$

where $V_{avg.ref}$ is the value of the average long-term wind speed at the height of measurement h_{ref}, h_0 – height of the forest and α is the approximation coefficient.

Similarly, to approximate the curve of height distribution for the average cubic long-term wind speed values $V_{avg.cub.h}$ the following expression could be used:

$$V_{avg.cub.h} = V_{avg.ref} \left(\frac{h}{h_{ref} - h_0}\right)^{\beta}, \quad (2)$$

where $V_{avg.cub.ref}$ is the value of the average cubic long-term wind speed at the height of measurement h_{ref}, and β is the respective approximation coefficient.

Figures 8 and 9 display, respectively, the curves of height h distribution for the average long-term wind speed values $V_{avg.h}$ and the curve of such distribution for the average cubic long-term wind speed values $V_{avg.cub.h}$. For wind shear modelling up to the height of 190 m expressions (1) and (2) are used on the basis of measurement data and extrapolation coefficients, which for Site 1 can be expressed as equations (3) and (4) [7]:

$$V_{avg} = 1.09 \cdot (h\text{-}10)^{0.39} \text{ (m/s)}, \quad (3)$$

$$V_{avg.\ cub} = 1.80 \cdot (h\text{-}10)^{0.30}, \quad (4)$$

and for Site 2 as equations (5), (6):

$$V_{avg} = 1.06 \cdot h^{0.36} \text{ (m/s)}, \quad (5)$$

$$V_{avg.cub} = 1.72 \cdot h^{0.29} \text{ (m/s)}. \quad (6)$$

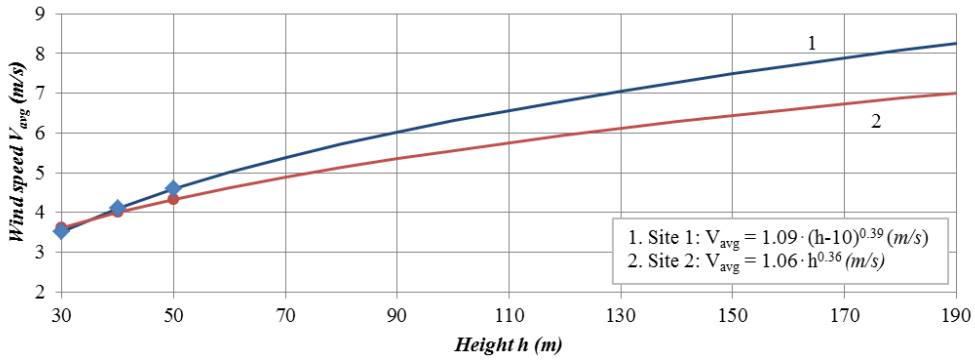

Fig. 8. The average long-term wind speed vs. height, $V_{avg.h} = f(h)$, for the sites 1, where $h_0 = 10$ *m*, and 2 extrapolated for the height up to 190 m using power law relationship (3), (5).

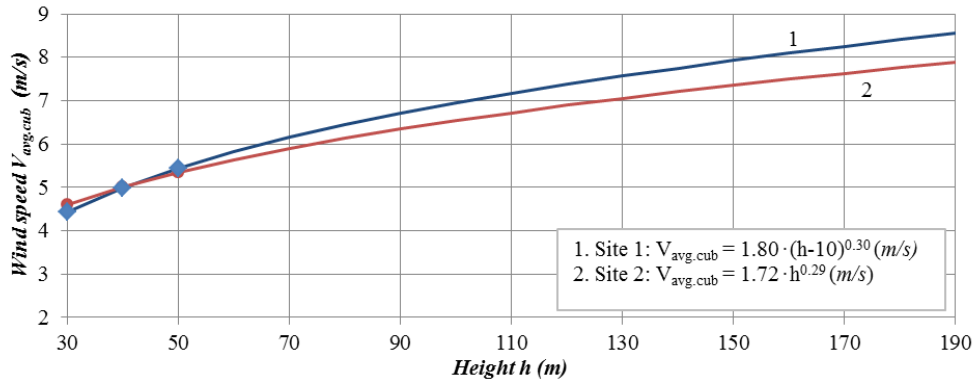

Fig. 9. The average long-term wind speed *vs.* height, $V_{avg.cub.h} = f(h)$, for the sites 1, where $h_0 = 10$ *(m)*, and 2, extrapolated for the height up to 190 m using power law relationships (4) and (6).

4. MAP OF POTENTIAL WIND ENERGY DENSITY IN LATVIA

Since 1945, systematic long-term wind speed measurement results at a height of 10 m have been stored in the archive of the Latvian Environment, Geology and Meteorology Centre. There are 24 sites, where wind speed monitoring takes place.

Distribution pattern of the average values of wind speeds in Latvia, obtained by analysing and summarising those long-term measurements, is presented in papers [8]–[10] in the form of different maps.

Based on these research materials about wind flow distribution and long-term wind shear investigations using measurement complexes at height up to 200 m, the authors developed the wind map shown in Fig. 10. This version of wind map allows for visual representation of wind speed distribution in Latvia divided into four zones I, II, III and IV, where different colours correspond to the different wind shear profiles.

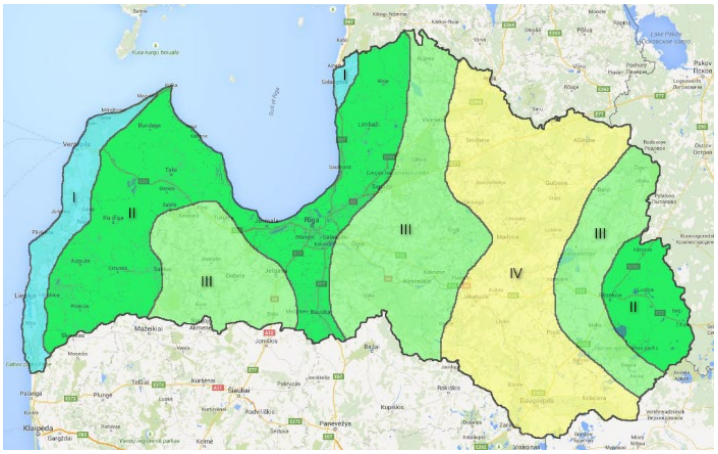

Fig. 10. Map for visual evaluation of distribution potential wind energy density in Latvia, where colours show regions with different average wind speed values V_{avg}, *(m/s).*

Tables 1 and 2 show average $V_{avg,}$ and average cubic $V_{avg\ cub}$ wind speed values at height of 30, 50, 100, 120, 140 and 160 m.

Value of average wind speed V_{avg} is calculated by expression

$$V_{avg} = 1/n \sum_{i=1}^{n}(V_i), \tag{7}$$

where V_i – wind speed value (m/s) for one measurement time (for measurement complex Symphonie – (3–5) s);

$i = 1, 2, 3...n$ – count of measurements.

Value of average cubic wind speed $V_{avg.cub}$ is calculated by expressions

$$V_{avg.cub} = \frac{1}{T} \sqrt[3]{\sum_{i=1}^{n}(V_i T_i)^3} \tag{8}$$

where V_i – wind speed value (m/s) for one measurement time;

T_i – measurement time (s);

$i = 1, 2, 3...n$ – count of measurements;

T – total measurement time, which is equal to sum of all measurements, calculated by expression

$$T = \sum_{i=1}^{n} T_i. \tag{9}$$

Table 1

Average Wind Speed V_{avg} Values for 4 Zones in Latvia at Heights h of 30, 50, 100, 120, 140 and 160 m

Zone	*h, m*	30	50	100	120	140	160
I	V_{avg}, *m/s*	3.6	4.6	6.3	6.8	7.3	7.7
II		3.5	4.5	5.7	5.9	6.3	6.8
III		3.4	4.0	4.9	5.2	5.5	5.7
IV		3.2	3.8	4.7	4.9	5.2	5.4

Table 2

Average Cubic Wind Speed $V_{avg.cub}$ Values for 4 Zones in Latvia at Heights *h* of 30, 50, 100, 120, 140 and 160 m

Zone	*h, m*	30	50	100	120	140	160
I	$V_{avg\ cub}$, *m/s*	4.7	5.5	7.1	7.5	7.9	8.2
II		4.6	5.3	6.5	6.9	7.2	7.5
III		4.5	5.1	6	6.3	6.5	6.7
IV		4.3	4.9	5.7	6.0	6.2	6.4

Values from Table 2 can be used for evaluation of wind flow energy intensity and calculation of wind turbine efficiency if installing them at different heights in different zones [11].

Within the ESF project a publicly available website (https://latwinddata.venta.lv/) has been developed for detailed visualisation of the collected wind data. Users can find basic information (average, min, max wind speed values per day) for the whole measured period, as well as the wind speed distribution curves are shown [12].

This website is dedicated for educational and research purposes allowing users to derive detailed information of wind parameters easily. In the future, it is planned to add wind data from other wind measurement devices and systems.

5. CONCLUSIONS

1. Results of long-term wind speed measurements using met masts of 50–60 m with registration unit LOGGER Symphonie 9200 and LIDAR complexes are presented on the map with four regions I, II, III and IV with different annual average wind speed values.
2. Results of wind shear measurements that are presented on the map are summarised in tables with values of average and average cubic wind speeds at heights of 30, 50, 100, 120, 140 and 160 m for each zone.
3. Publicly available website has been developed, where users can find basic information (average, min, max wind speed values per day) for the whole measured period, as well as the wind speed distribution curves are shown.

ACKNOWLEDGEMENTS

The research has been supported by the State Research Program "LATENERGI".

REFERENCES

1. Shipkovs P., Bezrukovs V., Bezrukovs Vl., Pugachevs V., and Silutins V. (2011). Measurements of the wind energy resource in Latvia. *World Renewable Energy Congress WREC 2011*, Sweden, 8–13 May 2011, Linköping, 0724 WE.
2. Bezrukovs V., Bezrukovs Vl., Shipkovs P., and Lizuma L. (2013). Investigation of wind energy distribution in height in Latvia. In *Proceedings of the 2013 ISES Solar World Congress*. Cancun, Mexico, 3–7 November 2013.

3. Bezrukovs, V., Bezrukovs, Vl., and Levins N. (2011). Problems in assessment of wind energy potential and acoustic noise distribution when designing wind power plants. *The 52nd International Scientific Conference on Power and Electrical Engineering*. Riga Technical University, October, 2011.
4. Bezrukov, V., Domburs, L., Pugachev ,V. (1995). The performance evaluation of the efficiency of the TW 600 wind power converter in Ainazi region. *Latvian Journal of Physical and Technical Sciences*, 2, 35–45.
5. Bezrukovs, V., Bezrukovs, Vl. (2012). Wind speed and energy at different heights on the Latvian shore of the Baltic Sea. *WREF 2012*, Denver, Colorado. Available at https://ases.conference-services.net/resources/252/2859/pdf/SOLAR2012_0214_full%20paper.pdf
6. Bezrukovs, V., Bezrukovs, Vl., and Lizuma, L. (2014). The landscape influence on the wind energy distribution in height on the Latvian shore of the Baltic Sea. *Energy Procedia*, 52, 223–233.
7. Bezrukovs, V., Zacepins, A., Bezrukovs, Vl., and Komashilovs, V. (2015). Assessment of wind shear and wind energy potential in Latvia. *Latvian Journal of Physics and Technical Sciences* 2, 26–39.
8. Vēja karte un kvalitāte. Available at http://www.kerveju.lv/veja_karte.php
9. Vēja ātrums 10 metru augstumā. Available at http://www.windenergy.lv/karte.html
10. Ostapenko J., and Gamalejevs A. (2004). Latvijas vēja enerģijas rokasgrāmata.
11. Bezrukovs, V., Bezrukovs, V., and Zacepins, A. (2014). Comparative efficiency of wind turbines with different heights of rotor hubs: Performance evaluation for Latvia. *Journal of Physics*: Conference Series 524 (2014) 012113, pp. 1–9.
12. Komashilovs V., Zacepins A., Bezrukovs V., Bezrukovs D., and Hofmanis J. (2014). Web application for processing and analysis of the raw wind measurement data. In *Proceedings of 15th IEEE International Symposium on Computational Intelligence and Informatics* (CINTI 2014), 19–21 November 2014, Budapest, Hungary, pp. 455–458.

VĒJA VERTIKĀLĀ PROFILA SADALĪJUMA PĒTĪJUMI BALTIJAS JŪRAS KRASTĀ

V. Bezrukovs, A. Zacepins, Vl. Bezrukovs, V. Komašilovs

Kopsavilkums

Rakstā ir dots apskats par vēja parametru mērīšanas kompleksiem un izpētes metodēm, kuri ir izmantoti dažādās vietās Latvijā ar mērķi novērtēt vēja enerģijas potenciālu. Balstoties uz ilglaicīgiem vēja vertikālā profila sadalījuma pētījumiem Baltijas jūras krastā, vēja ātruma sadalījuma likumsakarības ir demonstrētas līdz 160 metru augstumam. Rakstā ir prezentēti koeficienti, kuri ir lietoti vēja vertikālā profila ekstrapolācijai pēc jaudas likuma. Iespējamais vēja enerģijas sadalījums Latvijā ir parādīts kartes formā un tabulā ar vidējām kubiskām vēja ātruma vērtībām. Vēja parametru mērīšanas datubāze ir publiski pieejama tīmekļa vietnē.

04.03.2016.

LATVIAN JOURNAL OF PHYSICS AND TECHNICAL SCIENCES
2016, N 3
DOI: 10.1515/lpts-2016-0017

THEORETICAL AND EXPERIMENTAL INVESTIGATIONS OF CYLINDRICAL AIR-HEATING SOLAR COLLECTOR

I. Pelece[1], P. Shipkovs[2]

[1]Latvia University of Agriculture, 2 Liela Str., Jelgava, LV-3000, LATVIA
[2]Institute of Physical Energetics, 21 Aizkraukles Str., Riga, LV-1006, LATVIA
shipkovs@edi.lv

Solar energy is used not only at low latitudes, where it is available at large amounts, but also at higher latitudes, where height of sun and irradiance are significantly lower. On the other hand, the length of day at higher latitudes is longer in summer than at low latitudes, and also the path of the sun is longer.

The present research deals with seeking for new shapes of solar collectors capable of receiving more solar energy.

For designing and evaluating new shapes of solar collectors, it is necessary to have new methods for simple calculations of energy received from the sun by surface of any shape and direction. Such a method is explained in the present paper.

Based on calculations by the proposed method, a new form of solar collector – a cylindrical collector – has been worked out. This collector is intended for air heating, but main principles can also be used for water heating, and even for photovoltaics.

A cylindrical collector receives more energy in the morning and evening than a flat one, but at midday power of both collectors is equal, if effective areas are equal. Daily energy sum of the cylindrical solar collector is 1.5 times greater than that of the flat one.

Keywords: *air heating, collector, cylindrical, solar energy.*

1. INTRODUCTION

Along with other kinds of renewable energy, solar energy has been used not only at low latitudes, where it is available at large amounts, but also at higher latitudes, where height of the sun and, therefore, irradiance are significantly lower. On the other hand, the length of the day at higher latitudes is longer in summer than at low latitudes, and also the path of the sun is longer (for example, at the sixtieth degree of latitude during the summer solstice it is from 41^0 to 319^0, but the length of day is 17 h 51 min). Therefore traditional solar devices used in southern countries are not appropriate in higher latitudes, and new kinds of solar collectors and other devices must be developed.

In general, there are two ways to improve solar collectors. The first one is to seek for new better materials for the absorber and transparent cover for better use of the received energy. There are very many investigations in this direction (Kadirgan 2006; Siwulski et al. 2005; Hobbi & Siddiqui 2009). But there is also another way – to improve geometry of the collector to receive more energy. In this direction there is much less research mainly devoted to tracking systems and concentrators (Chong & Wong 2009). Traditionally the positioning of the collector and the tilt angle are understood with the geometry of the collector, but actually also the shape of the absorber itself can be better than flat. There are only few works, for example, (Abdulhadi & Ghorayeb 2006; Kurtbas & Durmus 2007) dealing with new shapes of collectors. Traditional flat-plate solar collector is capable of receiving solar energy approximately from 160º wide angle that corresponds to approximately 10 hours of work. Energy gain in the morning and evening is small. This problem can be solved by using the sun tracking flat-plate collector, but such mechanisms are expansive and moving parts need special maintenance and are not durable against wind. The present research deals with seeking for new shapes of solar collectors capable of receiving more solar energy during all day and from all sides.

Traditionally efficiency has been used for characterising a solar collector. Efficiency is defined as ratio between thermal power produced by the collector to that received by collector from the sun. But the efficiency really does not characterise energy gain from the collector. For calculation of the energy gain it is also necessary to know the amount of energy received by the collector that in some situations (especially when the collector is not flat) can be a rather complicated task. Efficiency characterises only materials and technologies used in construction of the collector, but not the geometry and positioning of it. For example, efficiency of a flat-plate solar collector will be the same when a collector is positioned horizontally or in the optimal slope, while energy gain can differ 1.4 times (Slama 2009). Hence, efficiency is not usable when we try to get more energy by changing shape and positioning of the collector, and new ways for characterising the solar collectors must be used. We suggest using coefficient of proportionality between the energy gain from a solar collector and the sum of global solar energy at the same period of time.

For designing and evaluating new shapes of solar collectors, it is also necessary to have new methods for simple calculation of energy received from the sun by surface of any shape and direction. Such method has been proposed in the present research.

Based on calculations by the offered method, a new form of solar collector – a cylindrical collector – has been worked out. Such a collector has been made and measurements of energy production have been carried out. This collector is intended for heating air, but main principles can be used for water heating as well, and even for photovoltaics (PV). Cylindrical solar collector has several advantages in comparison with the traditional flat-plate one: it receives solar radiation from all sides during the day, even if the length of day is 17 hours; it does not contain moving parts; it is more durable against wind than a flat-plate collector.

2. MATERIALS AND METHODS

2.1. New Method for Calculating Received Energy

2.1.1. Coordinates of the Sun

The first step to calculate energy received by some surface is calculation of coordinates at which the sun is seen in the sky. Height of the sun and azimuth are easy to use.

Coordinates of the sun can also be find at some Internet pages (for example, "http://ssd.jpl.nasa.gov/horizons.cgi," n.d.), but such a sheet is not convenient for use in further calculations, formulae are more appropriate.

Therefore, we obtained such formulae from astronomical considerations, using coordinate transformation formulae between several coordinate systems (Zagars & Vilks 2005). After few transformations we obtain sinus of the height of the sun:

$$\sin\delta = \left(\cos s \cdot \cos\chi + \sin s \cdot \sin\chi \cdot \cos\varepsilon\right) \cdot \cos\varphi + \sin\chi \cdot \sin\varepsilon \cdot \sin\varphi ,$$

where δ is the height of the sun, s is sidereal time, χ is ecliptic length of the sun, ε is slope of the earth axis (23°) and φ is latitude of the place. The sidereal time s can be assumed with good accuracy as

$$s = \left(\left(N - 81\right) \cdot 24 / 365.25 + t + 12 + \lambda\right) \cdot \pi / 12 ,$$

where N denotes the day of the year counted from 1 January, t is time within the day in hours, and λ is longitude of the place.

The ecliptic length χ in the first approximation can be assumed as

$$\chi = \frac{N - 81}{365.25} \cdot 2\pi .$$

It means a full circle in year, but a year in astronomy starts at the spring point. Then, if we know $\sin\delta$, $\cos\delta$ can be obtained from simple geometrical formula

$$\cos\delta = \sqrt{1 - \sin^2\delta} .$$

The trigonometric functions of the azimuth A of the sun can be calculated as follows:

$$\sin A = \frac{\sin s \cdot \cos\chi - \cos s \cdot \sin\chi \cdot \cos\varepsilon}{\sqrt{1 - \sin^2\delta}} \text{ and}$$

$$\cos A = \frac{\left(\cos s \cdot \cos\chi + \sin s \cdot \sin\chi \cdot \cos\varepsilon\right) \cdot \sin\varphi - \sin\chi \cdot \sin\varepsilon \cdot \cos\varphi}{\sqrt{1 - \sin^2\delta}} .$$

More detailed presentation of this method is given in (Pelece 2011). Later also other authors (Xiaoyan 2012) used a very similar method.

2.1.2. Energy Received by Surface

Solar radiation received by some surface consists of the direct or beam radiation and the diffused one. In general, direct radiation received from the sun on horizontal flat surface can be written as

$$R = R_0 \cdot P^m \cdot \sin\delta,$$

where R_0 is solar constant (1367±7 W/m^2, from "ISO 9488:1999(E/F) 3.24,"), P is lucidity of the atmosphere, in our case taken as constant and equal to 0.78 (Pelece et al. 2010), but m is atmosphere mass – a quantity characterising thickness of the atmosphere, which solar rays pass through in relative units compared with when the sun is at the zenith. It has been found (Young 1994) that the mass of the atmosphere with good accuracy (error 2 % percent at horizon, higher even less) can be expressed as

$$m = \frac{1.002432 \cdot \cos^2\theta + 0.148386 \cdot \cos\theta + 0.0096467}{\cos^2\theta + 0.149864 \cdot \cos\theta + 0.0102963 \cdot \cos\theta + 0.000303978},$$

where Θ is zenith angle of the sun, i.e. distance of the sun from the zenith, therefore $\cos\theta = \sin\delta$.

If receiving surface is not horizontal and/or is not flat, the main formula is $I = I_0 \cdot \cos\alpha$, where I is the intensity of solar radiation received by surface, I_0 is that on surface perpendicular to sun rays and α is the incidence angle of solar rays on surface, i.e., angle between sun rays and surface normal. If we know the height of the sun δ, azimuth of the sun A, slope of the surface (or surface element, if the surface is not flat) β and azimuth of the surface normal B, then $\cos\alpha = \sin\delta \cdot \cos\beta + \cos\delta \cdot \sin\beta \cdot \cos(A - B)$. As we know *sinA* and *cosA*, but not the azimuth A, we can use formula $\cos(A - B) = \cos A \cdot \cos B + \sin A \cdot \sin B$. Then we obtain

$$I = I_0 \cdot (\sin\delta \cdot \cos\beta + \cos\delta \cdot \sin\beta \cdot (\cos A \cdot \cos B + \sin A \cdot \sin B)),$$

where $I_0 = R_0 \cdot P^m$. For calculation of energy received by some surface within some time, this value must be integrated by surface (in the case of flat surface it means multiplying by surface area) and by time. Integrating by time is rather complicated, because both height and azimuth of the sun depend on time, and so does air mass. Therefore, numerical integrating can be used.

The other part of the global solar radiation is the diffused one. As several authors, for example, (Chikh et al. 2012) denote, usually only global radiation has been measured and therefore the diffused one must be evaluated theoretically. From several works it follows that the diffused radiation can be in good approximation considered as constant: Mghouchi et al. (2014) found it is 50 W/m^2, Andersen et al. (2015) found it to be 120 W/m^2 and Ahwide et al. (2013) found that in summer the diffused radiation is 100 W/m^2. Therefore, we consider the diffused radiation to be constant and equal to 100 W/m^2.

2.1.3. Effective Area

In some cases, especially if only the total received radiation, not its distribution, is required, calculations can be even more simplified using the effective area. The effective area of some surface, independently of its shape and orientation, is equivalent to the area of its projection on plane perpendicular to solar rays (or area, at which the receiving surface can be seen in direction of solar rays). Then radiation received by some surface is

$$I = I_0 \cdot S_{ef} \ ,$$

where I_0 is the radiation on plane perpendicular to solar rays and can be calculated

$$I_0 = R_0 \cdot P^m$$

as explained in Section 2.1.2, and S_{ef} is the effective area of the receiving surface.

For example, the effective area for a flat-plate collector is $S_{ef}=S\cdot\cos\alpha$, where α is the incidence angle of solar rays on surface, and solar radiation received by this collector is $I=I_0\cdot S_{ef}$.

2.2. Cylindrical Air-Heating Solar Collector

We suggest a new kind of solar collector – a cylindrical solar collector. The main idea is that the absorber is cylindrical and receives solar radiation from all sides. The axis of the cylinder is positioned perpendicularly to the orbital plane of the earth to ensure perpendicular incidence of sun rays on the absorber.

In our case it is an air heating solar collector, but such form of the absorber can be used for water heating as well, and even for photovoltaics. Our cylindrical air heating solar collector (Fig. 1, Fig. 2) consists of two coaxial cylinders: the inner cylinder is made of black-painted metal (galvanized 0.5 mm thick steel sheet coated with black mat silicon colour), and the outer one is made out of a transparent 1 mm thick PET material coated with UV-protective film.

Fig. 1. Cylindrical solar collector.

Such construction forms two spaces – the inner one inside the metallic cylinder, and the space between the metallic cylinder and the transparent one – where air can be heated. Diameter of the inner cylinder is 0.59 m, the outer 0.67 m, the length of both cylinders is 1.3 m.

Both cylinders are mounted on one axis positioned at South – North direction and the Northern end is lifted at 90º angle minus height of the sun at midday (pointed to the Polar star) to ensure perpendicular striking of solar beams to the collector surface all day long. Ends of the cylinders are closed with metal discs, covered with 3 cm thick Rockwool heat insulation from inside. There are openings in the discs for inflow of cold air and outflow of heated air. These openings are positioned so that inflow is at the bottom of the lower end of the cylinder and outflow is at the top of the upper end of the cylinder. Such positions allow convection-provided flow of air without a fan. All of these openings consist of two channels and a valve, allowing the use of heated air from the inner cylinder and from the space between the metallic cylinder and the transparent one, either together or separately.

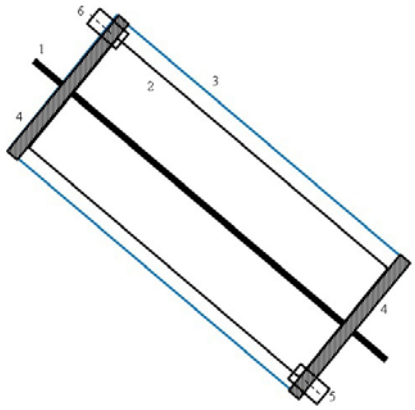

Fig. 2. Structure of cylindrical solar collector: 1 – axis, 2 – inner cylinder – absorber, 3 – outer transparent cylinder, 4 – thermoinsulation at ends, 5 – inflow opening, 6 – outflow opening.

An electrical fan was used to increase the air flow through the collector and, therefore, also its efficiency. For autonomy, the fan was powered from solar energy (photovoltaic). Such an approach can also ensure almost constant temperature of heated air due to decrease in air flow when intensity of solar radiation decreases, which in other cases can be ensured by using complicated automatics.

The temperature of inflowing and outflowing air was measured with data logger HOBO-H08-007-02 after every 2 minutes. The total air flow was measured using flowmeter Lutron YK-2001TM. Then the energy outcome from the collector Q can be calculated: $Q = c \cdot m \cdot \Delta T$, where c is specific heat of the air, m is mass of the heated air and ΔT is the difference between inflowing and outflowing air temperatures. The mass of heated air can be obtained: $m = p \cdot V / \left(R \cdot T \cdot \mu\right)$, where p is air pressure, V is volume, R is universal gas constant and μ is molecular weight of air. The volume is product of flow rate with cross-sectional area of the tube and time. The fan we used ensured velocity of air flow of 4 m/s at clear sun conditions, which for air inflow and outflow channels (diameter equal to 8 cm) gave air flow of 0.02 m^3/s or 72 m^3/h.

For the evaluation of the proportionality between energy gain from the collector and solar energy, the global solar energy was measured using ISO 1-st class Kipp&Zonen piranometer CMP 6 (positioned horizontally). Measurements were taken automatically after every 5 minutes.

3. RESULTS AND DISCUSSION

3.1. Calculated Daily Course of Power of Cylindrical Solar Collector

The daily course of power of cylindrical solar collector was calculated using methodology explained in Section 2.1.2 and compared with that of a flat plate collector positioned at the slope corresponding to maximum power at midday. Results are shown in Fig. 3.

As it was expected, cylindrical collector received more energy in the morning and evening than a flat one, but at midday power of both collectors was equal, if effective areas were equal. Daily energy sum of the cylindrical solar collector is 1.5 times greater than that of the flat one. Of course, real surface area of this cylindrical collector is larger than that of the flat one, but for the flat collector it is necessary to insulate back-side, while the cylindrical collector does not require it. Also the space occupied by the collector can be an important factor to decide in favour of the cylindrical one.

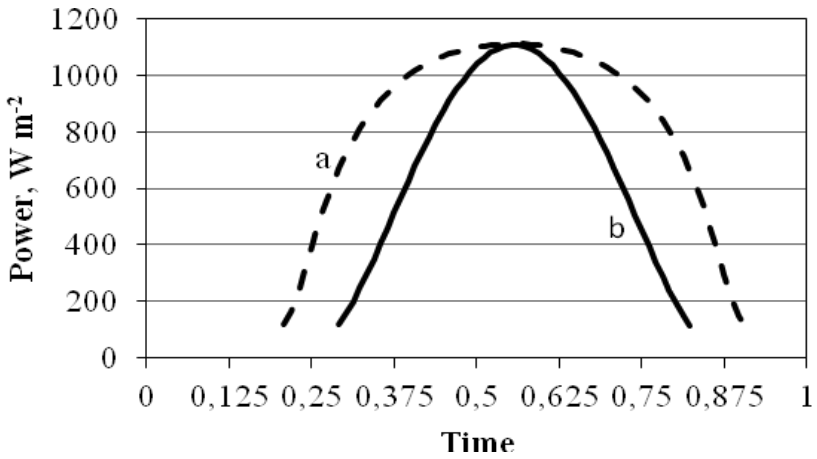

Fig. 3. Daily course of power of cylindrical (a) and flat (b) solar collectors.

3.2. Temperature of Heated Air

Measured temperature of outflowing air from a cylindrical solar collector gives similar results as calculations. Daily course of temperature of heated air together with intensity of global solar radiation at almost clear day (3 August 2015) is shown in Fig. 4.

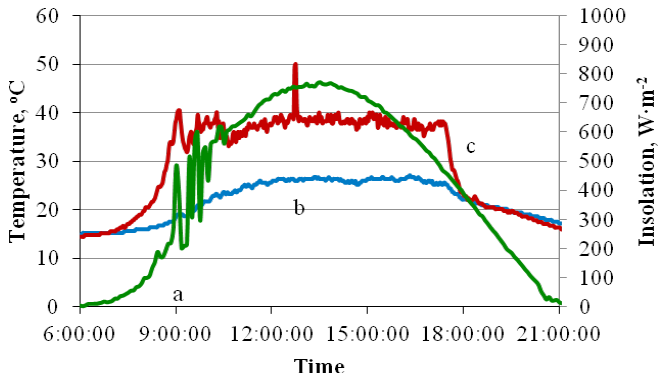

Fig. 4. Daily course of temperature of air heated with cylindrical solar collector at almost clear day (3 August 2015): a – solar radiation, W·m^{-2}; b – temperature of ambient air, ºC; c – temperature of heated air, ºC.

As seen from Fig. 4, temperature of the heated air reached 35 ºC soon after sunrise and remained almost constant during the day. Air flow under such sunny conditions was constant and equal to 4 m/s or 72 m^3/h. It resulted in daily mean power of the space between absorber and transparent coating 214 W, and of the space inside the absorber 192 W. In these measurements air flew through both these spaces; therefore, total daily mean power of the collector was 406 W. Such power is sufficient for drying of agricultural production. Similar results were also obtained at a partly cloudy day (Fig. 5).

Figure 5 shows daily course of temperature of the heated air together with the intensity of solar radiation at a partly cloudy day of 9 August 2015.

In this case, the temperature of heated air is even higher than at clear day, but this can be explained with accumulating of the warm air in the collector when the solar energy powered fan does not work due to clouds. This, in turn, means that such a fan powered by solar energy can be used instead of complicated automatics for ensuring approximately constant temperature of the heated air under partly cloudy conditions.

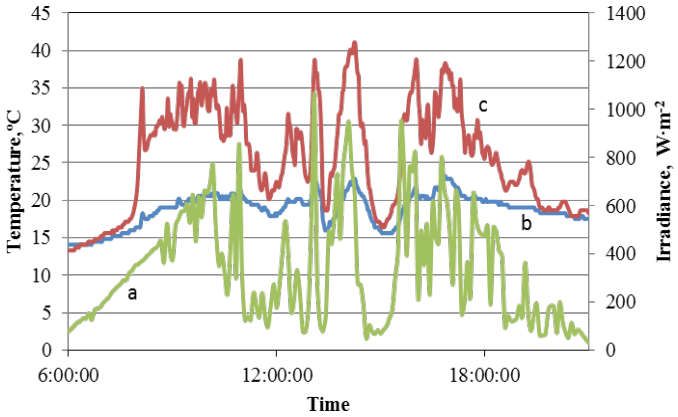

Fig. 5. Daily course of temperature of air heated with cylindrical solar collector at a partly cloudy day (9 July 2015): a – solar radiation, W·m^{-2}; b – temperature of ambient air, ºC; c – temperature of heated air, ºC.

Another interesting fact (Fig. 5) is that when clouds appear, solar energy among the clouds is higher than that of a clear day. It means that we receive not only direct radiation, but also radiation reflected from clouds, which, in general, is in the other direction than the direct one. Therefore, the cylindrical solar collector, which receives energy from all sides, has additional advantages in comparison with the flat one.

3.3. Daily Energy Gain from Cylindrical Solar Collector

In order to predict energy gain from a solar collector if global solar energy is known, the relevance between these two values must be studied (Pelece & Ziemelis 2012). Figure 6 shows a plot of dependence of daily energy gain from the cylindrical solar collector on daily sum of global (the direct radiation together with the diffused one) solar energy on 3–26 July 2015.

The graph shows direct proportionality between these values. Slope of linear trendline is the coefficient of proportionality, in this case 0.48, with coefficient of determination R^2= 0.78. These measurements were performed using only the space between the absorber cylinder and the transparent one (inner space of the absorber cylinder was closed from both ends). Similar results were obtained when only the inner space of the cylinder was used (space between absorber and transparent cover was closed). In this case, coefficient of proportionality was 0.52 with R^2= 0.86. Maximal coefficient of proportionality by using both spaces together was obtained, it was 0.63. In this case also the scattering of data was the smallest one – R^2 was 0.93. Such value of coefficient of proportionality means approximately 12 MJ or 3.3 kWh of energy at medium cloudy day in August, or heater with 500 W power during the day. Such power is sufficient for drying of agricultural production.

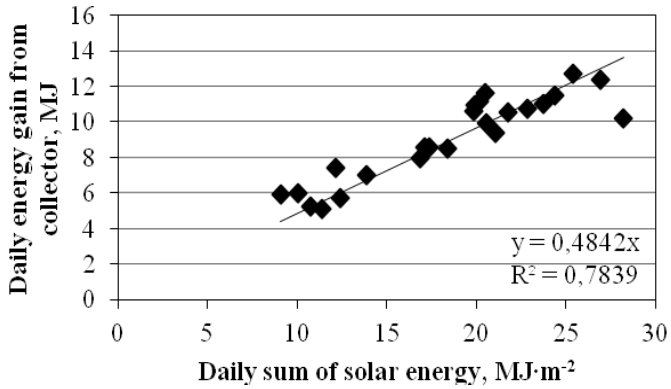

Fig. 6. Dependence of daily energy sums produced by cylindrical solar collector on those of global solar energy, 3–26 July 2015.

Large value of the coefficient of determination means that the coefficient of proportionality is only slightly dependent on solar radiation, cloudiness and other circumstances. Global solar energy depends on cloudiness, but the effectiveness of its use in a cylindrical solar collector is not affected by it.

4. CONCLUSIONS

There is a new simple method for calculation of received solar energy proposed in the present research. This method is mainly based on astronomical considerations on how to describe position of the sun in the sky. This method allows calculating the direct solar energy received by surface of any shape and position under clear-sky conditions, taking into account also atmosphere mass. It may be widely used for finding the best positioning of a traditional flat-plate solar collector (or photovoltaic) as well as for developing of new shapes of solar devices.

There is a new form of solar collector developed using this method – a cylindrical solar collector. The main advantage of such a collector is the possibility to receive solar energy from all sides and during all day, even if the length of day is 17 hours. This possibility can be compared to the sun tracking collector, but the cylindrical collector does not contain moving parts. Average power output of such an air-heating collector (diameter of 0.6 m and length of 1.3 m) is 500 W, or daily energy sum is 6 to 15 MJ (or 1.7 to 4.2 kWh) in August in Latvia. Such power is sufficient for drying of agricultural production. An air-heating collector has been considered in this article, but main ideas can also be used for water-heating collectors and even for photovoltaics.

REFERENCES

1. Abdulhadi, M.. and Ghorayeb, F. (2006). A self-tractable solar collector. *International Journal of Sustainable Energy*, 25(2), 63–78.
2. Ahwide, F., Spena, A., and El-Kafrawy, A. (2013). Correlation for the average daily diffuse fraction with clearness index and estimation of beam solar radiation and possible sunshine hours fraction in Sabha, Ghdames and Tripoli – Libya. *APCBEE Procedia*, 5, 208–220.
3. Andersen, E. et al. (2015). Measurements of the angular distribution of diffuse irradiance. *Energy Procedia*, 70, 729–736.
4. http://ssd.jpl.nasa.gov/horizons.cgi.
5. ISO 9488:1999(E/F) 3.24.
6. Chikh, M., Mahrane, A., and Haddadi, M. (2012). Modeling the diffuse part of the global solar radiation in Algeria. *Energy Procedia*, 18, 1068–1075.
7. Chong, K.K., and Wong, C.W. (2009). General formula for on-axis sun-tracking system and its application in improving tracking accuracy of solar collector. *Solar Energy*, 83, 298–305.
8. Hobbi, A., and Siddiqui, K. (2009). Optimal design of a forced circulation solar water heating system for a residental unit in cold climate using TRNSYS. *Solar Energy*, 83, 700–714.
9. Young, A.T. (1994). Air mass and refraction. *Applied Optics*, 33, 1108–1110.
10. Kadirgan, F. (2006). Electrochemical nano-coating processes in solar energy systems. *Hindawi Publishing Corporation International Journal of Photoenergy*, (Article ID 84891), 1–5.
11. Kurtbas, I., and Durmus, A. (2007). A comparison of a new type conical solar collector with a flat-plate solar collector. *e-Journal of New World Sciences Academy*, 2 (Article Number A0028 ISSN 1306-3111).

12. Meclouch, R.F., and Brahim, A. B. (2008). A global solar radiation model for the design of solar energy systems. *Asian Journal of Scientific Research*, 1(3), 231–238.
13. Mghouchi, Y. et al. (2014). New model to estimate and evaluate the solar radiation. *International Journal of Sustainable Built Environment*, 3(2), 225–234. Available at: http://www.sciencedirect.com/science/article/pii/S221260901400051X.
14. Pelece, I., Vanags, M., and Migla, L. (2010). Evaluation of atmospheric lucidity and diffused radiation. *Latvian Journal of Physics and Technical Sciences*, 6, 40–46.
15. Pelece, I., and Ziemelis, I. (2012). Water heating effectiveness of semi-spherical solar collector. In *Proceedings of International Scientific Conference "Renewable Energy and Energy Efficiency".* LLU, ISBN 978-9984-48-070-1, 185–188.
16. Siwulski, S., Nocun, M., and Gruszka, B. (2005). Glassy coating for solar energy conversion. *Optica Applicata*, 35(4).
17. Slama, R. B. (2009). Incidental solar radiation according to the solar collector slope – Horizontal measurements conversion on an inclined panel laws. *The Open Renewable Energy Journal*, 2, 52–58.
18. Zagars, J., and Vilks, I. (2005). *Astronomija augstskolam*, Riga, Latvia: LU.

CILINDRISKA GAISA SILDĪŠANAS SAULES KOLEKTORA TEORĒTISKIE UN EKSPERIMENTĀLIE PĒTĪJUMI

I. Pelēce, P. Šipkovs

K o p s a v i l k u m s

Saules enerģija tiek izmantota ne tikai dienvidu zemēs, kur tā ir pieejama lielos daudzumos, bet arī lielākos platuma grādos, kur saules augstums un starojuma intensitāte ir daudz mazāki. No otras puses, vasarā lielākos platuma grādos ir garāka diena, nekā dienvidos, un arī saules ceļš ir garāks.

Šis darbs veltīts pētījumiem par jaunām saules kolektoru konstrukcijām, kuras spēj saņemt vairāk saules enerģijas.

Jaunu saules kolektoru formu projektēšanai un novērtēšanai ir nepieciešamas arī jaunas virsmas saņemtās saules enerģijas aprēķinu metodes. Metode ir aprakstīta šajā darbā.

Balstoties uz piedāvātās metodes aprēķiniem, jaunas formas saules kolektors - cilindrisks kolektors - ir izstrādāts. Šis kolektors ir paredzēts gaisa sildīšanai, bet var tikt izmantots arī ūdens sildīšanai, kā arī fotoelementiem.

Cilindrisks kolektors no rīta un vakarā saņem vairāk enerģijas nekā plakans kolektors, bet pusdienas laikā kolektoru jauda ir vienāda, ja efektīvie laukumi ir vienādi. Iegūtās enerģijas dienas summa no cilindriska saules kolektora ir 1,5 reizes lielāka nekā no plakanajam.

19.04.2016.

LATVIAN JOURNAL OF PHYSICS AND TECHNICAL SCIENCES
2016, N 3
DOI: 10.1515/lpts-2016-0018

WAVE ENERGY POTENTIAL IN THE LATVIAN EEZ

J. Beriņš[1], J. Beriņš[2], J. Kalnačs[3], A. Kalnačs[4]

[1] Faculty of Power and Electrical Engineering, Riga Technical University, 1 Kalku Str., Riga, LV – 1658, LATVIA
[2] Faculty of Computer Science and Information Technology, Riga Technical University, 1 Kalku Str., Riga, LV – 1658, LATVIA
[3]Institute of Physical Energetic, 21 Aizkraukles Str., LV – 1006, Riga, LATVIA
[4] LLC Environment, Bioenergetics and Biotechnology Competence Centre, 21 Aizkraukles Str., LV – 1006, Riga, LATVIA

The present article deals with one of the alternative forms of energy – sea wave energy potential in the Latvian Exclusice Economic Zone (EEZ). Results have been achieved using a new method – VEVPP. Calculations have been performed using the data on wave parameters over the past five years (2010–2014). We have also considered wave energy potential in the Gulf of Riga. The conclusions have been drawn on the recommended methodology for the sea wave potential and power calculations for wave-power plant pre-design stage.

Keywords: *Latvian EEZ, renewable energy, sea wave potential, wave energy, wave energy distribution of time wave energy directional distribution.*

1. INTRODUCTION

Up till now, sea waves are an untapped source of energy in Latvia. Wave energy is a renewable resource, which is increasingly used worldwide. Its volume can be estimated between 80,000TWh and 8,000TWh [1]. Several authors believe that wave energy could also become one of the most promising energy sources for electricity generation in our country [2], [3]. For wave energy to be captured and transformed, wave power stations are required. Technical solutions that determine whether they will be profitable are dependent on specific local conditions. To find them, an objective assessment of wave energy potential is required. The following factors are essential for this assessment:

1. The potential amount of energy;
2. Wave expansion in different directions;
3. Wave energy variability over time.

To meet this challenge, the following is required:

1. Wave output parameter data of the maritime area of interest;
2. An optimal wave energy calculation method;
3. The calculation of results and their analysis and evaluation.

2. THE MAIN CHARACTERISTICS OF SEA WAVES

Sea waves along the Latvian coast of the Baltic are irregular. Wave height, period and wave propagation direction are random variables. Choosing sufficiently short intervals and a small enough surface on the sea, for example, 1m x 1m we can assume that this parameter (wave height, period and direction of spread) change can be described by means of probability theory as a stationary random process. In this case, calculating the energy potential is the most appropriate wave frequency[1] power density spectrum *S (f),* [4]. The spectrum of our case is characterized by the following parameters:

H_s – characteristic wave height = H_{m0} (m);

T_z – average wave period (zero crossing) = T_e (s)[2];

T_p – the wave period, which corresponds to the maximum energy of the spectrum;

θ_{vid} – average angle of wave propagation direction.

Characteristic wave height – ***swh (significant wave height)*** wave parameters in meters, which characterize irregular wave water surface fluctuations and determine the energy density spectrum. *swh* is used in a variety of wave energy and power calculations in deep, medium and shallow water. Elsewhere this parameter is represented by the H_s. Historically, the characteristic wave height is the average wave height of 1/3 of the maximum wave period examined (see Fig. 1) [5].

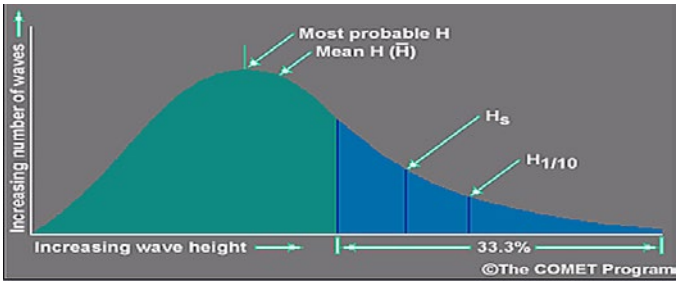

Fig. 1. Definition of characteristic wave height illustration [5].

It is believed that the characteristic wave height H_s is shown more precisely by H_{m0} than by $H_{1/3}$ [6, p. II - 1 - 88 (5)]. H_{m0} is obtained by processing the power density spectrum *S(f)* according to the expression:

$$m_0 = \int_0^\infty S(f)df \ , \tag{1}$$

where: $m_{o\,t}$ – the 0-th spectral moment, random variable or variate 0-th moment is constant, the determined auxiliary value uses different variant values, including H_{m0} the calculation being:

$$H_{m0} = 4\sqrt{m_0} \ , \tag{2}$$

Average wave period T_z – wave parameters in seconds characterized by irregular wave water surface fluctuations and by the energy density spectrum. Since it is less than or equal to the energy wave period T_e, wave energy and power evaluation are used in calculations.

T_e – wave power density spectrum average energy periods, the energy density range of -1 and 0 consecutive moments linking the relationship $T_e = m_{-1}/m_0$.

m_k, or k – the spectral moments – is defined as:

$$m_k = \int_{f-0}^{\infty} f^k S(f)\, df \tag{3}$$

K-th order spectral moment is a specific constant determining the shape characteristics of the set of points applied in the mechanics and statistics (probability distributions and spectra) (m_1 mechanics – the sum of mass = center of mass, m_2 – rotational inertia), where k can be: -4 -3, ..., 0, 1, 2, 3, 4

Main wave direction mwd (mean wave direction) – wave parameter in degrees, which is characterized by irregular wave water surface fluctuations and energy directional spectrum. It is used in areas with real or notional receiver lines for wave energy potential evaluation. This is the direction which the waves come from in any prevailing wave period (DPD) [7]. Output data *mwd* is assigned as the azimuth.

3. DESCRIPTION OF THE FIRST DATA USED IN CALCULATIONS

The following criteria were used to select Control Points:

1. Sea area *"A"* (see Fig. 2) – the eastern Baltic Latvian exclusive economic area (EEA) waters are 216 km long and 95 km wide;
2. South-western and western winds in this area are prevailing [8]; [13], and therefore the direction of the waves is an important source of wave energy;
3. South-western and western winds are also prevailing in the eastern part of the Gulf of Riga – so it was decided to expand the project's initial task of examining the wave potential not only in maritime area *"A"*, but also in maritime area *"B"* (see Fig. 3);
4. Area *"B"* – the eastern part of the Gulf of Riga could be a potential wave energy source;
5. We chose six control points in the Baltic Sea area *"A"* by the Latvian coast, and one point of the Gulf of Riga opposite Salacgriva – area *"B";*
6. The selected C*ontrol Point* coordinates and their existing depths are shown in Table 1, and the visual location on the map in Fig. 3;
7. Most of the waves will not be longer than 70 m. This means that the minimum depth is 17.5m, as up to 95 % of the wave energy is dispersed in the layer between the water surface and depth equal to a quarter of the wave length [9], [10].

Table 1

Coordinates and Depth of Chosen Control Points

Control point No.	Coordinates	Debth, m
1	56.060, 20.898	24
2	56.503, 20.810	18
3	57.048, 21.234	24
4	57.421, 21.381	56
5	57.645, 21.601	21
6	57.746, 24.184	31
7	56.400, 20.810	24

Fig. 2. Illustration of distribution of Control Points.

It is possible to indirectly determine statistical data of wave parameters in areas such as the Baltic Sea EEZ Latvian west coast, where measurements have not been made in sufficient quantity and quality to allow for the assessment of the energy potential of the region. It is based on data on wind direction and strength, and the corresponding processing algorithm adjustment points where the comparison of results with direct measurements are possible [14]. We use data based on the Danish Meteorological Institute (DMI) wave model adjusted to the program SWAN. They are received by using a special modelling program, processing satellite data on wind direction and speed as well as satellite data on wave height. Since we do not have local technical resources, which provide the data for the spectrum parameter adjustment, we will use wave energy density spectrum characteristic parameters [10]. They are H_s *(swh)*, T_z and MWD data collected over the previous five years (2010–2014).

For the wave energy potential calculation we will use the raw data from seven Control Points (see Fig. 2). The basic data of the calculation are the sea wave energy density spectrum characteristic parameters of the seven Control Points at given depths for every hour of 24 hours a day, every day of the month and every month – 12 months of the year, every year, for five consecutive years (2010–2014). Assuming that the meteorological and hydrological conditions in our chosen area are sufficiently homogeneous, the calculated results can be related to the adjoining sea +/- 5km. DMI data are in increments of about 10 km [6].

From the wave start / input data, it is evident that the *mwd* values are reviewed every 1˚ in the 360˚ spectrum. Moreover, this parameter indicates only the dominant, but not all wave directions each hour.

4. METHOD OF CALCULATION CHOSEN

The simplest method is to calculate the specific wave power and wave energy at separate points in the area [2], [3].

The following method: a defined wave receiver line is drawn in the sea (a straight line segment or several segments at shallow angles) [10], and the entire energy flow calculated through a vertical plane passing through the line receivers in one direction. Each wave direction energy flow and the direction of wave energy during the distance unit would fall *cos θ* times, where θ – the angle at which the wave front forms with the defined receiver line.

The whole border of the area serves as the vertical surface receiver across the whole depth of energy release. Cumulative flow of energy per year (TWh) is determined by the average wave power P_{vid} (kW/ m) or wave of energy flow through the surface – EPRI (Electric Power Research Institute) methodology [16].

These methods have some obvious shortcomings:

1. Assessment of the potential energy depends on the relative receiver line placement, because it determines the angle θ, on which it depends, as to how much the energy potential assessment decreases;
2. It is an energy assessment of the potential of the notional receiver lines and so there is no energy assessment of the potential of the area, as it does not allow for the possibility that the receivers' mutual positions could be changed, which would be a normal strategy in the case of an increase in perceptible energy, when receivers would automatically reorientate or be reorientated to working position;
3. Even assuming the direction of wave energy distribution spectrum can be described as a narrowband spectrum, angle *mwd* does not describe the amount of all incoming energy, but only part of the amount;
4. If you use the border area method, problems in evaluating wave energy arise due to wind changes in this area.

In order to mitigate these shortcomings in the assessment of wave energy, we offer the wave energy direction baseline projection (VEVPP) method.

1. On the energy spectrum by integrating the frequency range [0; ∞], we calculate the average wave energy density J_{vid} of time interval of 1m^2 field:

$$J_{vid} = \rho g \int_0^\infty S(f)df = \rho g m_0 = \frac{\rho g \left(Hm_0\right)^2}{16} = \frac{\rho g \left(Hs\right)^2}{16} \tag{4}$$

where: ρ – sea water density s, kg/ m^3; g – gravity acceleration, m/ s^2; f – wave frequency, *Hz*; *S(f)* – wave energy spectrum function; m_0 – 0th spectral moment;

$H_{m0} = H_s$ – characteristic wave height, m; The wave phase velocity – c_g in deep water:

$$c_g = c_f, \tag{5}$$

where: c_f – wave phase velocity; T – average wave period T_z (zero crossing); as mentioned above, it is replaced by T_e (s).

The wave average power in a 1m wide wavefront or wave energy flow through the vertical plane perpendicular to the wave direction of movement is expressed as:

$$P_{vid} = J^*_{vid} \cdot c_g \tag{6}$$

Consequently, irregular wave energy, crossing the plane perpendicular to the direction of movement of the wave, in a time interval on a 1m wide wavefront is expressed as:

$$E = P^*_{vid} \tag{7}$$

According to (7), specific calculations of wave energy are performed in each of the 6 selected control points at n (time) intervals.

2. The Baltic Sea area *"A"* is perpendicular to 8 traditional wind and wave axes (*PVxx* where: *xx* = (*N, NE, E, SE, S, SW, W and NW*). We set baselines perpendicular to the direction. Thus, we have 4 lines which intersect each other at one point and cross the border area from 4-way baseline segments *BNyy* where *yy* = (*N-S, E-W, NE-SW, SE-NW*) (Fig. 3).

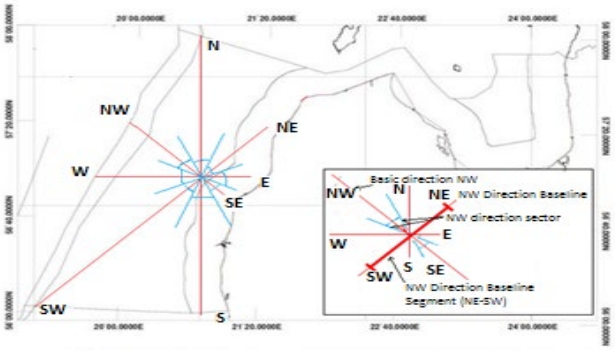

Fig. 3. Basic wave direction sea area *"A"* base line segments [11].

3. On line segment BNyy we construct and fix perpendicular control point Km, where m = (1, 2, 3, 4, 5, 7) projections $Km_{\text{N-S}}$, $Km_{\text{E-W}}$, $Km_{\text{NE-SW}}$, $Km_{\text{SE-NW}}$.

4. We introduce a selective *mwd* directional filter at control points to assess specific wave energy directional distribution.

$$IF(mwd_i, PVxx_{min}, PVxx_{max}) = 1, \text{ if } PVxx_{min} < mwd_i \leq PVxx_{max}; \tag{8}$$

$$IF(mwd_i, PVxx_{min}, PVxx_{max}) = 0, \text{ if } mwd_i > PVxx_{max} \text{ or } PVxx_{min} \geq mwd_i. \tag{9}$$

5. Thus, the summation of wave energy direction (7) during time interval Δt in each of the control points by sector accounts for mutually non-duplicative direction of wave energy.

$$\dot{E}_n\left(KmPVxx\right)=\Delta t\cdot\frac{\rho g^2}{64\pi}\sum_{i=1}^{n}IF\left(mwd_i,PVxx_{\min},PVxx_{\max}\right)\left(Tei\left(Hsi\right)^2\right) \quad (10)$$

where: *PVxx* – one of the axes *xx* = (*N, NE, E, SE, S, SW, W, NW*); $PVxx_{min}$ – the key sector *PVxx* minimum limit; $PVxx_{max}$ – the key sector PVxx ceiling; $H_{si.}$ – characteristic wave height of i-th time interval Δt; $T_{e\,i}$ – i-th mean energy period of wave energy density spectrum; *PVxx* sector size is equal to $PVxx_{max}$ - $PVxx_{min}$=45˚, (see blue lines in Fig. 3).

In addition, the following summation of the direction of various wave energy by sectors reduces the errors that arise from the assumption that all the energy interval of time Δt point is associated with only one wave direction *MWD*.

As a result, we obtain the wave's specific energy assessment in xx (Ws), n intervals Δt (Δt = 1 hour, or 3600's) in eight basic sectors at each Control Point, which are attributed to the direction of the base cut-off point projection Km xx.

If the resulting energy is measured in kWh, then inserting Δt=3600 / 1000, ρ =1003kgm^3, g = 9.81m/s^2 and π = 3.14 rad cumulative energy can be expressed as:

$$\dot{E}_{n,m,xx,yy}480,32/10^3\cdot\sum_{i=1}^{n}IF\left(mwd_i,PVxx_{\min},PVxx_{\max}\right)\cdot\left(Ti\left(Hsi\right)^2\right) \quad (11)$$

This equation characterizes control point Km wave energy potential of the key *PVxx* projection point intervals of any specific baselines *PNyy*, where the number n may be the time interval of one month = 672h, if the month has 28 days, or one month = 744H if the month has 31 days.

One year Energy potential of Control Points K_m-th for a 1m wide wave front E_g is calculated as:

$$\dot{E}_{g,m,xx,yy}=\sum_{n=1}^{12}\left(En,m,xx,yy\right) \quad (12)$$

6. Thus, knowing basic sectors PV_{xx} specific energy values $\dot{E}n(Km_{xx})$, control projection points Km_{xx}, to get direction PV_{xx} specific energy curve, which corresponds to the base line segment, we execute the function approximation. Comparing different approximation method results, including fourth and fifth grade interpolation curves, we chose the horde method, which simplified the following specific energy integration process, without sacrificing the accuracy of the results.

This method consists of replacing points of some specific energy wave function with a straight length cutline of the polygon and the amounts in each direction of the basic line projection segment $\Delta L(K1_{xx}, K5_{xx})$.

7. Directional control baseline projection of corresponding energy can be calculated by integrating the distance within the projection of the specific energy function. Thus, the integration process reduces the expression to the trapezoidal method [14] used:

$$\begin{aligned}&Exxyy\left(K1,K5\right)=\sum_{m=1}^{m+1=7}E\left(\Delta L\left(m,m+1\right)xx\right)=\\&=\sum_{m=1}^{m+1=5}\frac{\dot{E}n\left(Km\right)+\dot{E}n\left(Km+1\right)}{2}\cdot\Delta L\left(m,m+1\right)xx\end{aligned} \quad (13)$$

where: *m* – control point projection Km_{xx} sequence number (1, 2, 3, 4, 5, 7); *m+1*– control point projection $Km+1_{xx}$ sequence number; *ΔL(m,m+1)* – the distance between the projection points to the direction of the base, taking into account the baseline azimuth and control coordinates (see Table 1).

8. Knowing the wave energy potential of the control area with the checkpoints *K1*; *K2; K3; K4; K5* and *K7*, which mark the control projection of the direction of the baselines (see Fig. 4), and knowing that the control area also represents a significant share of the test area *"A"* as well as taking into account the assumption that the wave energy distribution in time and space is uniformly distributed, we are able to evaluate each of the key *PVxx* amounts of energy, increasing in proportion to the direction of the baseline segment *PNyy* and control the projection pieces which total *L (K1, K5) yy* ratio.

9. The sum of 8 wave energy potential projections is the total wave energy potential per month / year.

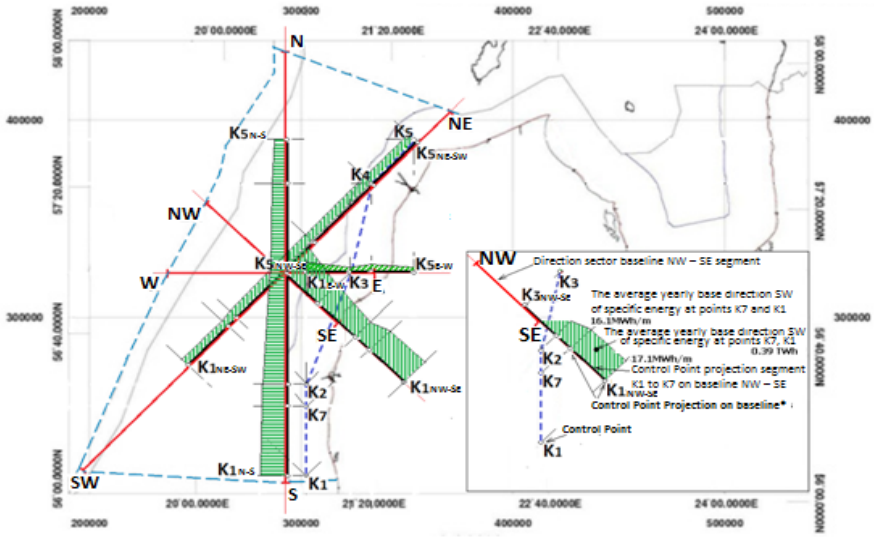

Fig. 4. The average annual wave energy direction projection of Baltic Sea Area *"A"*.

10. Since the VEVPP method includes calculations related to the outcomes of several control point placements in the plane, to evaluate the result we used a simpler method of wave energy assessment, defined in one of the selected control points (*K7*, the specific energy average volume over one year is close to the average of the test control group) specific energy in a special way related to the whole area. Their many time intervals - Δ*t* component $\dot{E}_n(n,\theta_n)$ are graded and summated using *mwd* through eight basic *PVxx* (*xx = N, NE, E, SE, S, SW, W, NW*) 45˚ sectors, gaining 8 average specific energy $\dot{E}_{g7,}xx$ components. Each component is multiplied by one of the corresponding four-base line piece lengths PN_{yy}, thus obtaining an approximate area of energy height-directional distribution assessment *Eg7(PVxx,PNyy) (yy = N-S, NE-SW, E-W,NW-SE)*. Summarizing, we obtain comparative average energy potential assessment over one year in Latvia's EEZ.

5. RESULTS OF LATVIA'S EEZ WAVE POTENTIAL CALCULATIONS

1. When using two methods – Z_0 and VEVPP, results were obtained for wave energy potential of Latvia's EEZ in the Baltic Sea area *"A"* (see Fig. 2) in accordance with 6.46 TWh / year and 6.51 TWh / year.

2. Using the wave energy direction distribution calculation method of receiver conventional directional line segment, the following results were obtained:

a) Average annual wave energy directional distribution in the reporting period;

b) The average amount of monthly breakdown of wave energy direction for each year during the reporting period;

c) The directional distribution of annual average wave energy volume;

d) The directional distribution of annual average wave specific energy in the reporting period (examples of control points *K5, K6* and *K7*, Fig. 8).

3. The calculations were made in 7 control points during the period of 2010-2014:

a) Hourly interval wave specific energy;

b) Monthly wave specific energy (examples of *K5, K6* and *K7* – Fig. 9);

c) The annual average specific wave energy (see Fig. 5).

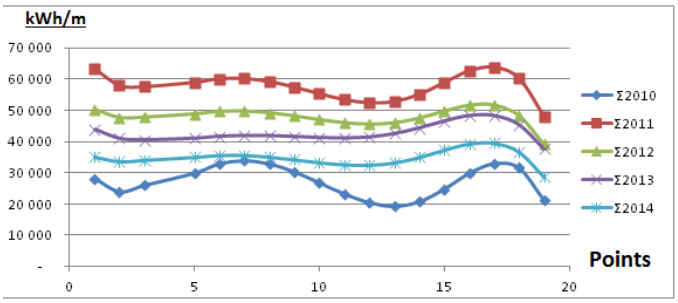

Fig. 5. Baltic Sea wave energy specific potential (2010–2014) points *N 1–N19* (kWh/m).

By summarizing the specific potential of the data on a monthly basis as well as by interpolating these results, the evaluation of the specific energy potential points *N1–N19* was obtained (Fig. 6).

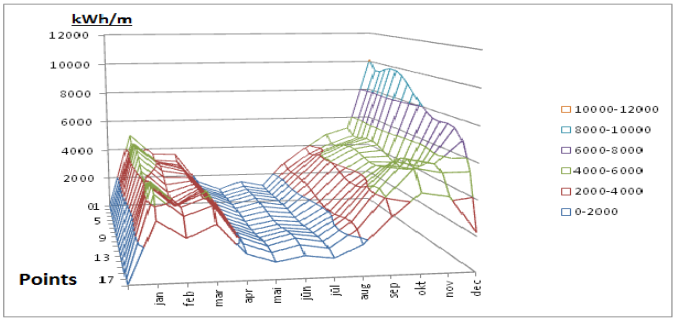

Fig. 6. Monthly average (2010–2014) of specific energy potential points *N1–N19* (kWh/ m).

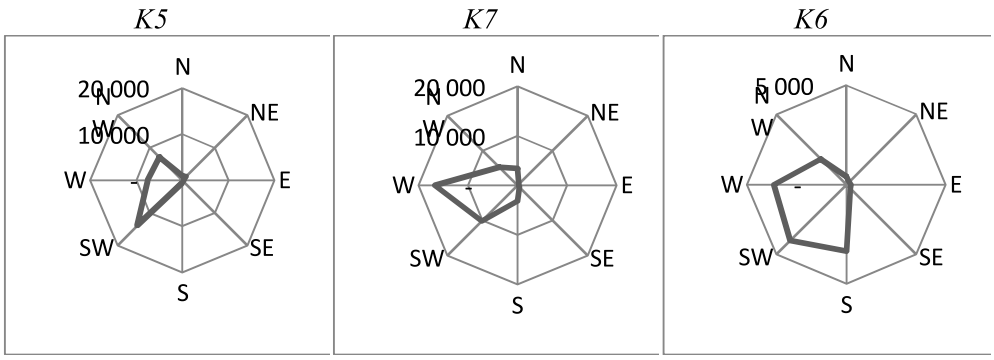

Fig. 7. The average of the specific energy direction distribution of Control Points *K5, K6* and *K7* (in kWh/ m).

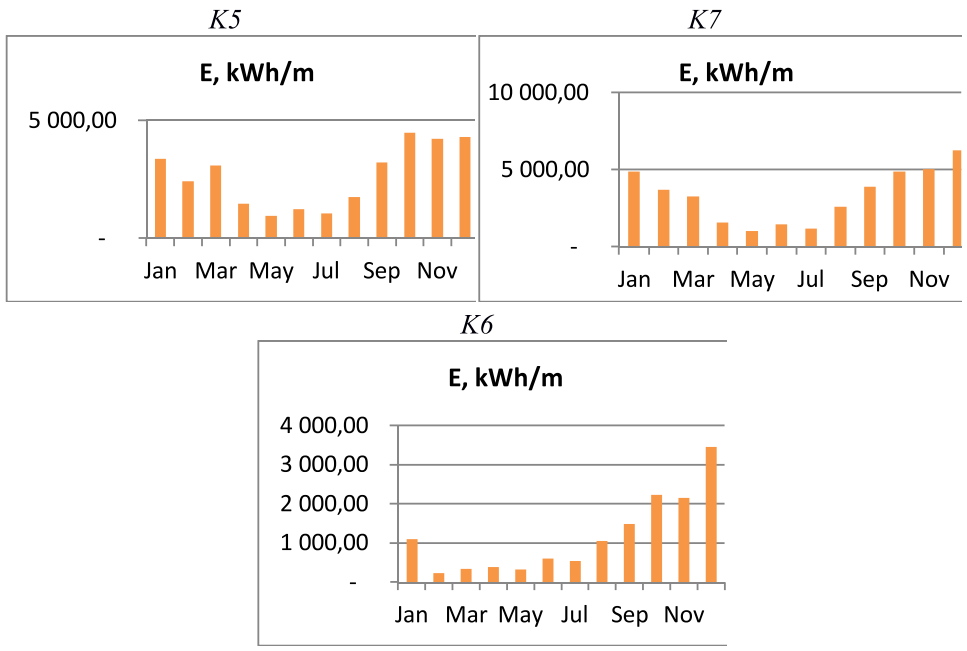

Fig. 8. Monthly breakdown of specific energy (kWh/ m) at Control Points *K5, K6* and *K7.*

6. CONCLUSIONS

1. The amount of wave energy in 1m wide waves in the Gulf of Riga is about 3 times less than the corresponding figure for the Baltic Sea Latvian EEZ. It is considered that the main causes are wave formation distances and ice formation conditions.
2. At least 90 % of the wave energy in the Baltic Sea Latvian part of the EEZ comes from the South West – West and North West axes.
3. The complicated energy direction distribution points to the fact that potential SWPS placement will depend on the receiver's functioning angle range.

4. Calculating the Baltic Sea Region *"A"* wave energy potential using VEVPP method the result is 6.51 TWh / year. Using comparative evaluation obtained by the method based on different control point principles of location, it is on average 6.46 TWh / year (- 0.77 %). The results are close which means that the new method of wave energy distribution assessment is plausible. Wave energy direction projection method compared to traditional methods more evenly and fully accounts for the different directions of energy in the area.

ACKNOWLEDGEMENTS

The research has been supported within Project No. L-KC/2.1.2.1/10/006, according to contract No. L-KC-11-0005 between Ltd "Vides, Bioenerģētikas un Biotehnoloģijas Kompetences Centrs" and Latvian Investment and Developement Agency (11th April 2011).

REFERENCES

1. Holmberg, H., Anderson, M., Bolund, B., and Stananger, K. (2011). Wave Power, Surveillance Study of the Development, Elforsk rapport 11: 02.
2. Beriņš, J., and Beriņš, J. (2015). Viļņu enerģētikas faktoru un attīstības perspektīvu analīze Latvija. *E&P 6.*
3. Avotiņš, A., Greivulis, J. and Kalniņš, L. (2008). Baltijas jūras potenciāls viļņa enerģijas pārveidošanai. *Enerģētika un Elektrotehnika* 23, ISSN 1407-7345.
4. Prat, M.C. (2008). Owerwiew of Ocean Wave Statistics. Available at https://upcommons.upc.edu/bitstream/handle/2099.1/6034/06.pdf?sequence=7
5. Comet Met Ed. Available at https://www.meted.ucar.edu/sign_in.php?go_back_to=https%3A%2F%2Fwww.meted.ucar.edu%2Fmarine%2Fmod1_wv_type_char%2Fnavmenu.php%3Ftab%3D1%26page%3D5.2.1%26type%3Dtext##
6. DMI Ocean and Ice services. DMI WAM model. Available at http://ocean.dmi.dk/models/wam.uk.php
7. National Data Buoy Center. Available at http://www.ndbc.noaa.gov/measdes.shtml
8. Bojārs, E. (2009). Aizsargājamās jūras teritorijas Ņida-Pērkone. Dabas aizsardzības plāns. Available at http://www.daba.gov.lv/upload/File/DAPi_apstiprin/AJT_Nida-Perkone09.pdf
9. Guiberteau, K.L., Liu, Y., Lee J., and Kozman, T.A. (2012). *Investigation of Developing Wave Energy Technology in the Gulf of Mexico*. Available at http://www.aeecenter.org/files/newsletters/CWEEL/WaveEnergy.pdf
10. Soomere, T. and Eelsalu, M. (2016). On the wave energy potential along the Eastern Baltic Sea coast. *E&P 6.*
11. JONSWAP. Available at http://www.codecogs.com/library/engineering/fluid_mechanics/waves/spectra/jonswap.php
12. MK noteikumi. Nr.779 (17.08.2010.). Noteikumi par bāzes līniju punktu koordinātēm.
13. Soomere, T., and Keevallik, S. (2001). Anistropy of moderate and strong winds in the Baltic Proper. *Proc. Estonian Acad. Sci. Eng.* 7(1), 35–49.

14. Zviedris, A. (2004). *Datorrealizācijas matemātiskās metodes.* Lekciju konspekts. RTU 78.
15. World Meteorological Organization. (1998). Guide of Wave Analysis and Forecasting. 702. Available at https://www.wmo.int/pages/prog/amp/mmop/documents/WMO%20No%20702/WMO702.pdf
16. Jakabson, P. (2011). *Mapping and Assessment of the United States Ocean Wave Energy Electric Power Research Institute.* Technical report. Available at http://www1.eere.energy.gov/water//pdfs/mappingandassessment.pdf.

VIĻŅU ENERĢIJAS POTENCIĀLS LATVIJAS EEZ

J. Beriņš, J. Beriņš, J. Kalnačs, A. Kalnačs

K o p s a v i l k u m s

Raksts ir par vienu no atjaunojamās enerģijas veidiem, kurš nerada būtisku piesārņojumu – jūras viļņu enerģiju. Konkrētāk, par šīs enerģijas potenciālu Latvijas EEZ (ekskluzīvā ekonomikas zonā). Tā noskaidrošanai lietota jauna metode. Aprēķinu veikšanai ir lietoti piecu gadu (2010. – 2014.) dati – viļņu augstumi, periodi un virzieni. Apskatīts arī viļņu enerģijas potenciāla aprēķins Rīgas Jūras līcī. Izdarīti secinājumi par ieteicamo metodiku viļņu spēkstaciju pirms-projektēšanas potenciāla un jaudu aprēķiniem.

02.05.2016.

LATVIAN JOURNAL OF PHYSICS AND TECHNICAL SCIENCES
2016, N 3
DOI: 10.1515/lpts-2016-0019

INVARIANT CONTROL OF THE TECHNOLOGICAL PLANTS TO COMPENSATE AN IMPACT OF MAIN DISTURBANCES PREEMPTIVELY

A. Sniders, A. Laizans, T. Komass

Latvia University of Agriculture, Faculty of Engineering,
Institute of Energetics
5 J. Cakstes Blvd., Jelgava, LV-3001, LATVIA

The paper considers a survey of the research procedures and results due to invariant control method application perspective for operation quality advancement in several technological plants (wastewater biological treatment tanks and water steam production boilers), which operate under influence of organised and random disturbances. A specified subject of research is the simulation model of the multi-link invariant control system for steam pressure stabilisation in a steam boiler by preemptive compensation of steam load and feed water flow impact on output parameter (steam pressure), developed in MATLAB/SIMULINK. Simulation block-diagram of the steam boiler invariant control system, containing closed loop PID control circuit and open loop DPC circuit, has been composed on the basis of the designed mathematical model of the system components, disturbance compensation algorithms, and operational equation of the invariant control system. Comparative response of the steam boiler, operating under influence of fluctuating disturbances, with conventional PID control and using PID-DPC control with disturbance compensation controller DPC, has been investigated. Simulation results of invariant PID – DPC control system show that output parameter of the steam boiler - pressure remains practically constant under fluctuating disturbances due to a high-speed response of DPC controller.

Keywords**:** *controller, disturbance, invariant control, simulation model, steam boiler, technological plant, wastewater aeration.*

1. INTRODUCTION

It is crucially important to have an appropriate option of technological processes and plant automatic control method and technical solution. It allows reducing operation costs due to minimisation of energy consumption, as well as increasing process stability and overall quality using an optimally selected control strategy. A topicality of urban environment is waste processing, including industrial and communal wastewater treatment, which accounts for a large part of municipality budget.

Wastewater cleaning is provided by biologically active sludge – a complex set of live cells, bacteria and microbes, which consume the waste. In order to facilitate

metabolism, oxygen must be supplied and dissolved in the wastewater. Wastewater cleaning quality is controlled indirectly – by measuring oxygen concentration in water at the exit from cleaning facilities. Oxygen is supplied to the aeration tank using air blowers driven by variable-frequency electric motors. Thus, the inverter output frequency is the response to the dissolved oxygen concentration measured at the aeration tank exit [1]. As a wastewater aeration system is the main energy consumer – up to 80 % of wastewater processing plant, high control parameter level substantially increases the energy consumption and total expenses.

The main task of aerator control system is to keep dissolved oxygen concentration high enough – usually around $2 g \cdot m^{-3}$ [1], [2]. Major perturbation that has direct impact on oxygen concentration over all aeration tank volume is variable wastewater afflux, and waste concentration in incoming wastewater. Research shows that wastewater concentration is affected by a precipitation level, and people's daily and weekly activity (variation is more than 200 %) [2], and wastewater afflux fluctuates by more than 40 % on a daily basis, and by 50 % on a monthly basis (mean monthly wastewater afflux for a town with 7000 inhabitants fluctuates from 800 m^3 (December) to 1600 m^3 (April) [3]).

If the dissolved oxygen concentration is too low, sludge metabolism stops, and wastewater is not cleaned. If low oxygen concentration occurs often and for long time, active sludge components die. It can take 3–6 months to restart a wastewater cleaning process. As this is a risk factor which has very strong negative impact, wastewater plant operators usually keep the dissolved oxygen concentration much higher than necessary – between 3 and $4 g \cdot m^{-3}$. Such extremely high set points tremendously increase energy consumption and generate additional expenses.

PID controllers are widely used for wastewater aeration process automation, but the research shows low control quality and inability to respond adequately to both main perturbation variations because of several variables to be controlled [1], [2]. This is also the reason of keeping high dissolved oxygen concentration set points at the aeration tank exit. Simulation and experimental research have proven that an invariant control system can keep dissolved oxygen concentration near the set point with fluctuation less than ± 3% [4], and it reduces the energy consumption by more than 30 % without any additional investments.

The additional challenges for wastewater aeration automatic control system designers are fluctuating inertia and sensitivity of the wastewater aeration tank [4]. Aeration tank inertia is between 40 and 90 minutes, depending on afflux and aeration tank size, sensitivity changes with waste concentration and waste composition. Adaptive PID-DPC control system, the parameters of which are correctly calculated according to the invariant control principle, cancels out the impact of perturbations – fluctuating waste concentration and afflux [1], [2].

The other technological facilities with high impact of disturbances are the steam boilers as the energy conversion units, which transform the combustion energy of fuel into steam heat and mechanical power. High pressure steam boilers are applied in cogeneration plants. Low pressure steam is used for technological needs and autonomous heating of food production enterprises.

Main tasks of the steam boiler design, operation and automatic control are as

follows: 1) to minimise heat losses from the furnace and boiler room using economizers, increasing heat resistance and fuel combustion efficiency, as well as optimising heat load control; 2) to reduce flue gas emissions using emission reduction facilities and applying burners optimal control; 3) to continuously measure, analyse and control inner technological parameters – steam pressure and temperature, drum water level and temperature, as well as main disturbances – feed water flow and steam flow that have direct impact on output parameters.

Conventional PID control is still the current tool for the steam boiler control [5]. The main control loop with only PID controller cannot eliminate an impact of disturbances efficiently enough because of delayed response to variable steam expenditure and feed water flow.

To increase operation stability and process control quality of the steam boilers and power plants, wide investigations of long-range control methods have recently been made: an active disturbance rejection control method, using multi-variable robust controllers with robustness against uncertainties and disturbances [5], [6]; an adaptive PID & Fuzzy logic control for transient process optimisation [7]; an automatic reservation to compensate extreme overloads [8].

New approaches on the subject of development of the heat power unit-turbine control technology are complex control using linear hybrid automata [9] and invariance of multi-variable control [10]. General concept of steam boiler control improvement by active disturbance rejection is invariant control. Main advantages of this control method are verified in the simulation model of steam boiler output variable (steam pressure) control, invariant to steam flow [11].

The basic task of the given research is to develop and investigate the mathematical and simulation model of disturbance invariant PID-DPC control system for steam boiler, insensitive to variations of steam load and feed water flow.

2. RESEARCH SUBJECT AND METHODS

Research subject is the model of two-disturbance invariant control system of the steam boiler VAPOR TTK-70 with closed loop control link of steam pressure p(t), open loop control link of steam expenditure $q_s(t)$ and open loop control link of feed water supply $q_w(t)$ as the main disturbances of steam pressure.

The algorithms of the disturbance preemptive compensation (DPC) controller are compiled according to the invariant control principle in strong correlation with the algorithms of steam boiler and power supply unit, as well as steam flow and feed water flow impact on steam pressure. The transfer functions and operational equations of the steam boiler control system components are composed using mathematical analyses and operator mathematics.

For simplicity, heat transfer in the steam boiler is analysed as a process, where steam pressure changes uniformly with time, not position. Then the transient process can be described by the ordinary differential equations. Simplified linear model of steam boiler is used for no-load mode ($q_s(t) = 0$ and $q_w(t) = 0$), as well as linear models of disturbances impact for a limited area of their changes.

Technical parameters of steam boiler VAPOR TTK-70 are as follows: heat

power – 2 MW; rated steam capacity – 50 kg· min^{-1}; max steam pressure – 10 bar; drum water capacity – 7700 kg; steam temperature – 184 °C; feed water temperature – 90 °C; OILON burner GKP- 250M – (0.37–2.6) MW.

A functional block-diagram of invariant PID-DPC control system is shown in Fig. 1. Main control loop consists of the PID controller, the frequency converter and the actuator for power flow regulation, the controllable technological plant and the sensitive transducer for output parameter measurement and conversion.

To realise an invariance of the output parameter control, apart from variations of main disturbances D1 and D2, the disturbance controller DPC is introduced. According to measurement results of disturbance D1 and D2, the controller DPC produces output signal X_{pc} for preemptive activation of frequency converter. Thereby, an actuator corrects the regulation impact – power flow in time and eliminates an output parameter change.

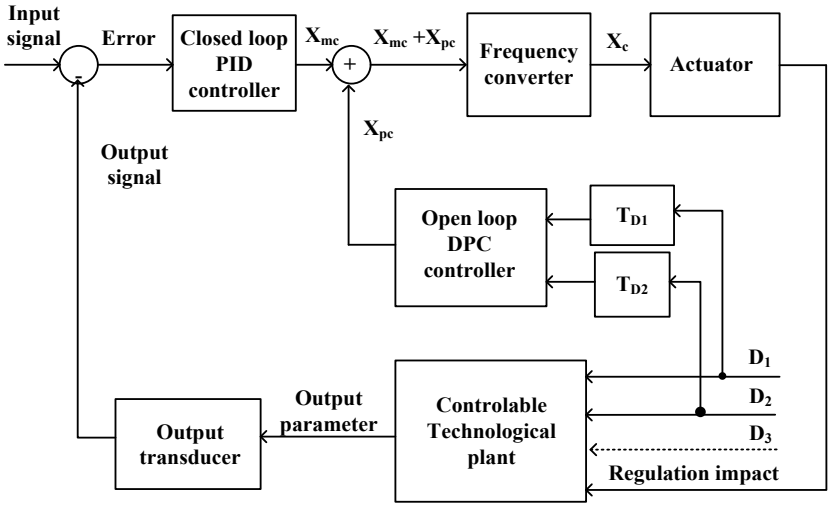

Fig. 1. Functional block-diagram of invariant PID – DPC control system: X_{mc} – main control signal;X_{pc} – preemptive control signal; X_c –frequency converter output signal; D_1, D_2 , D_3 – disturbances; T_{D1}, T_{D2} – transducers for main disturbances measurement.

3. MATHEMATICAL AND SIMULATION MODELS

The conventional algorithm of the PID controller, available in SIMULINK, is used. All constants of PID controller are tuned automatically during simulation process (Fig. 2). For no-load mode ($q_s = 0$, $q_w = 0$) the steam boiler is considered to be two component volume (water + steam) unit with constant sensitivity and response parameters. In that case the transient process of pressure alteration can be described by second-order transfer function:

$$G_{sb}(s) = \eta_{sb} \cdot p_0(s) \cdot Q_f(s)^{-1} = \eta_{sb} \cdot K_{sb} \cdot [T_w \cdot T_s \cdot s^2 + (T_w + T_s) \cdot s + 1]^{-1}, \quad (1)$$

where $Q_f(s)$, $p_0(s)$ – Laplace transforms of furnace heat flow and steam pressure at no-load mode; $\eta_{sb} = 0.93$ – efficiency factor of the boiler, using economizer; $K_{sb} = 11.5$ bar·MW^{-1} – transfer coefficient of steam boiler at ideal no-load mode; $T_w = 5$ min, $T_s = 19$ min – time constants of water and steam volumes.

Variable steam expenditure q_s as a load has a directly negative effect on steam pressure in the boiler. Load growth causes pressure decrease for transient volume Δp_{qs}. This can be described by the following second order transfer function:

$$G_{q_s}(s) = \Delta p_{qs}(s) \cdot q_s(s)^{-1} = K_{qs} \cdot [\tau_{qs} \cdot T_{qs} \cdot s^2 + (\tau_{qs} + T_{qs}) \cdot s + 1]^{-1}, \quad (2)$$

where $q_s(s)$, $\Delta p_{qs}(s)$ – Laplace transforms of steam flow and steam pressure change; $K_{qs} = 0.135$ bar·min·kg^{-1} – transfer coefficient of steam flow impact on steam pressure; $\tau_{qs} = 5$ min, $T_{qs} = 7$ min – dead time and time constant of steam flow.

Feed water flow q_w is regulated by frequency controlled centrifugal pumps in correlation with the steam expenditure and causes additional change of common steam pressure in the boiler for transient volume Δp_{qw} that can be described by the following second order transfer function:

$$G_{q_w} = \Delta p_{qw}(s) \cdot q_w(s)^{-1} = K_{qs} \cdot [\tau_{qw} \cdot T_{qw} \cdot s^2 + (\tau_{qw} + T_{qw}) \cdot s + 1]^{-1}, \quad (3)$$

where $q_w(s)$, $\Delta p_{qw}(s)$ – Laplace transforms of feed water flow and steam pressure change; $K_{qw} = 0.038$ bar·min·kg^{-1} – transfer coefficient of feed water flow impact on steam pressure; $\tau_{qw} = 2$ min, $T_{qw} = 7$ min – dead time and time constant of feed water flow impact.

The heat power actuator consists of frequency converter; servomechanism with servomotor and feedback for stability improvement, gas and air valves; and furnace. According to the block-diagram (Fig. 2), the transfer function of the actuator input-output link for transient process simulation is compiled:

$$G_a(s) = Q_f(s) \cdot i_a(s)^{-1} = [K_{fb}^{-1} \cdot (K_{gv} + K_{av}) \cdot K_f] \cdot [(K_c \cdot K_{sm} \cdot K_{fb})^{-1} \cdot s + 1]^{-1} = K_a \cdot (T_a \cdot s + 1)^{-1}, \quad (4)$$

where $i_a(s)$, $Q_f(s)$ – Laplace transforms of actuator input signal and furnace heat flow; $K_c = 2.5$ Hz·mA^{-1} – transfer coefficient of frequency converter; $K_{fb} = 4.5$ mA·rad^{-1} – transfer coefficient of servomechanism feedback; $K_{sm} = 0.063$ radians · min^{-1} · Hz^{-1} – speed coefficient of servomotor; $K_{gv} = 2.5$ m^3·min^{-1}·rad^{-1} – transfer coefficient of gas valve; $K_{av} = 24$ m^3·min^{-1}·rad^{-1} – transfer coefficient of air valve; $K_f = 0.043$ MW·m^{-3}·min – transfer coefficient of furnace; $K_a = 0.24$ MW·mA^{-1} – transfer coefficient of actuator; $T_a = 1.4$ min – time constant of actuator response.

Main task of the steam boiler control system is to ensure perfect compensation of the physical impact of variable steam expenditure $q_s(t)$ and feed water flow $q_w(t)$ on steam pressure $p(t)$ by using the disturbance preemptive compensation controller, which operates according to the invariant control principle.

The mathematical model of steam boiler invariant control system, containing a steam pressure closed loop PID control circuit and steam flow, and feed water flow open loop DPC control circuits, is the following operational equation:

$$p(s)=[i_0(s)\cdot G_{PID}(s)\cdot G_a(s)\cdot G_{sb}(s)+(K_{sf}\cdot G_s(s)\cdot G_a(s)\cdot G_{sb}(s)-G_{qs}(s))\cdot q_s(s)+$$
$$+(K_{wf}\cdot G_w(s)\cdot G_a(s)\cdot G_{sb}(s)-G_{qw}(s))\cdot q_w(s)]\cdot(K_p\cdot G_{PID}(s)\cdot G_a(s)\cdot G_{sb}(s)+1)^{-1}, \quad (5)$$

where $q_s(s)$, $q_w(s)$ – Laplace transforms of main disturbances (steam flow and feed water flow); K_{sf}, K_{wf} = 0.2 mA·kg^{-1}·min – transfer coefficients of steam and feed water flowmeters; G_s (s), G_w (s) – unknown transfer functions of steam and feed water disturbances controller.

In conformity with the invariant control principle, the following conditions of the process invariance can been formulated: if $K_{sf}\cdot G_s(s)\cdot G_a(s)\cdot G_{sb}(s)-G_{qs}(s)=0$ and $K_{wf}\cdot G_w(s)\cdot G_a(s)\cdot G_{sb}(s)-G_{qw}(s)=0$, then the disturbances q_s *(t)* and q_w *(t)* do not affect the transient process in the steam boiler.

Considering that $T_a<0.1T_{sb}$, the algorithms of the disturbance (steam expenditure and feed water flow) preemptive compensation controller DPC should be composed according to such transfer functions:

$$G_s(s)=G_{qs}(s)\cdot(K_{sf}\cdot G_a(s)\cdot G_{sb}(s))^{-1}\approx 0.245\cdot(130\cdot s^2+25\cdot s+1)\cdot(35\cdot s^2+12\cdot s+1)^{-1} \quad (6)$$

$$G_w(s)=G_{qw}(s)\cdot(K_{wf}\cdot G_a(s)\cdot G_{sb}(s))^{-1}\approx 0.071\cdot(130\cdot s^2+25\cdot s+1)\cdot(35\cdot s^2+12\cdot s+1)^{-1} \quad (7)$$

The transfer functions (6), (7) describe conditions of disturbance impact on steam boiler preemptive compensation. The block-diagram is compiled in SIMULINK for the steam boiler control system simulation and transient process comparative analysis of conventional PID control model and invariant PID-DPC control model with disturbance controller (Fig. 2).

The main closed loop control circuit consists of the following models: a "PID Controller" model with limited output (± 20mA), auto-tuning of control circuit parameters and activated Wind-up function for transient process optimisation; an actuator model for heat power supply regulation with operation algorithm (4) ("Converter", "Servomotor" with "Feedback" to improve the control stability; "Air Valve" and "Gas Valve" for gas mixture flow regulation on "Furnace"); a "Steam boiler" model composed as a subsystem with operation algorithms of heat flow regulation effect (1), steam flow disturbance effect (2) and feed water flow disturbance effect (3) on steam pressure; a "Pressure transducer" for steam pressure continuous measurement.

For simulation of heat flow effect on steam pressure an open access – free access SIMULINK model of the steam boiler transfer function (1) is compiled, using closed loop circuits with integrators and math operation blocks that make possible to enter the model parameters – process sensitivity and dynamics indices (transfer coefficients and time constants) during all the simulation time.

Main advantage of open access structure is a possibility to make an adaptive self-tuning model for adequate simulation of non-stationary technological process if sensitivity and dynamics indices of the technological unit are not constant, but vary with disturbances substantially [12].

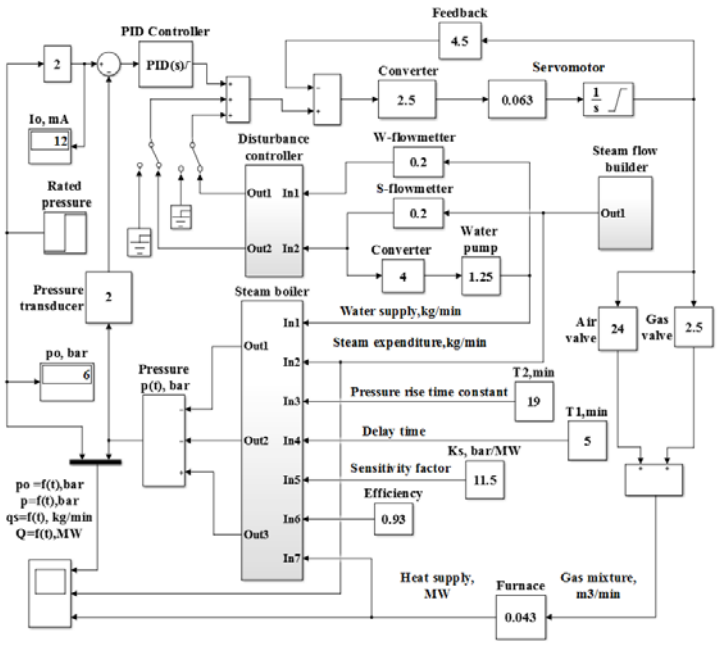

Fig. 2. Simulation block-diagram of steam boiler PID – DPC control system.

To perform constant, linear, pulse case and randomly changing components of steam flow $q_s(t)$ (kg/min), as a load and main disturbance of the steam boiler, a "Steam flow builder" model is applied.

The simulation model of the "Disturbance Controller" DPC is performed according to algorithms (6), (7) as coupled second order differential filters. Steam flow and feed water flow are measured by "S – flowmeter" and "W – flowmeter". To minimise disturbance on steam pressure, the feed water flow to steam boiler has been delivered continuously in close correlation with steam expenditure flow, applying "Water pump" with frequency "Converter" controlled asynchronous electrical drive, whose productivity rate is 1.25 $kg \cdot min^{-1} \cdot Hz^{-1}$.

4. SIMULATION PROCEDURES AND RESULTS

Simulation comparative results of the steam boiler conventional PID control system and invariant PID – DPC control system are presented in Fig. 3. To search for a wide spectrum of steam flow $q_s(t)$, as a load on steam boiler, influence on the steam pressure p(t), the simulation time should be long enough because of high steam pressure transient process time ($t_{tr} \geq 4T_{sb} \approx 4 \cdot 19 = 76$ min).

Simulation is started at no-load mode with zero disturbances (steam load $q_s(t) = 0$ and feed water flow $q_w(t) = 0$). Afterwards, the transient steam pressure reaches set point – 6 bar and becomes stable, the linear growing load (rise ramp 3.3 $kg \cdot min^{-2}$) from zero to rated value - 50 $kg \cdot min^{-1}$ is activated. To search for steam boiler reaction on steam flow large and fast perturbations, a linear growing overload (+40 % of rated value) and linear changing under load (-40 % of rated value) are added. After 100 minutes from the start, a random component with amplitude ± 10 % of rated value and frequency 0.5 min^{-1} is added ($q_s(t)$ in Fig. 3).

Simulated response of steam pressure p(t) change in the steam boiler feedback control system with optimally tuned PID controller shows that the overshoot of the steam pressure run up process is below 10 % and response time does not exceed 20 minutes. Under fast growing load from zero to rated value, the steam pressure response curve has the maximum deviation up to 50 %. Under linear and step case load variations (± 40 % of rated value) $p(t)$ maximum deviations reach up to ± 25 % of rated value (p_1(t) in Fig. 3). It testifies that the feedback control system with PID controller is sufficiently stable and fast in operation under no-load or constant load conditions, but operation quality is insufficient under substantially variable load. Due to response inertia of PID controller, the heat power regulation is delayed and therefore is not efficient enough ($Q_1(t)$ in Fig. 3) and disturbance rejection is too late that cause great deviations of control parameter p_1 (t).

Activation of steam pressure $p(t)$ main disturbance (steam expenditure as a load of the steam boiler) compensation link of the Disturbance controller ("Out 2" in Fig. 2), operation algorithm of which (6) is compiled in accordance with the invariance conditions, shows that maximum deviation of rated steam pressure (6 bar) decreases from 50 % to 14 % in comparison with only PID control ($p_2(t)$ in Fig. 3). Disturbance impact on the steam pressure is substantially eliminated by efficient regulation of the heat power flow ($Q_2(t)$ in Fig. 3).

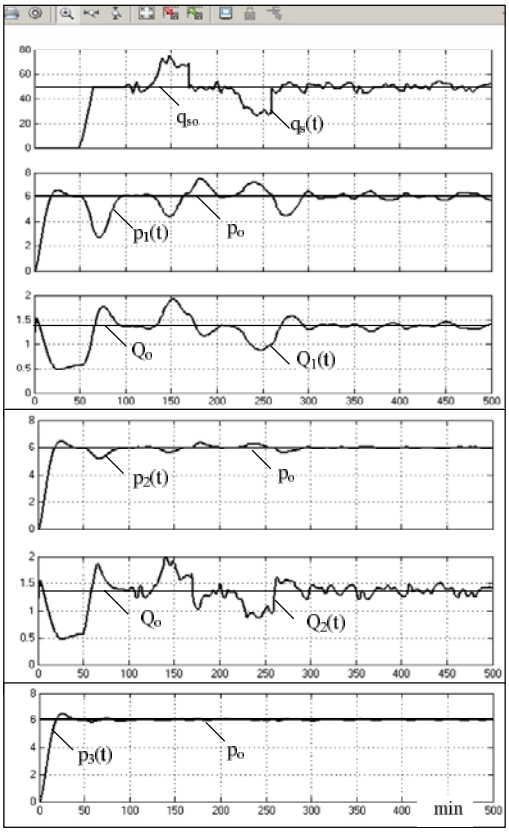

Fig. 3. Transient characteristics of the steam pressure p (t)(bar) and heat flow $Q(t)$ (MW) control model under randomly varying steam flow $q_s(t)$ (kg/min) and water flow $q_w(t)$ (kg/min): $p_1(t)$, $Q_1(t)$ – PID control; $p_2(t)$, $Q_2(t)$ – (PID + DPC) control invariant to $q_s(t)$; $p_3(t)$ – (PID + DPC) control invariant to $(q_s(t)+ q_w(t))$; p_0, Q_0, q_{s0} – rated values of main technological variables.

Simulated response of steam pressure invariant PID-DPC control system with two disturbance $(q_s(t)+q_w(t))$ preemptive compensation controller, the parameters of which are calculated and tuned according to the invariant control algorithms (6, 7), shows that the process parameter $p(t)$ remains practically constant under any type of steam expenditure – constant, steady changing, pulse or randomly fluctuating (p_3 (t) in Fig. 3). If the steam flow deviates by ± 25 % from the rated value, deviations of the steam pressure do not increase by ± 3 % of set point value. High quality of steam pressure stabilisation is reached due to fast and synchronous compensation of disturbance impact on control transient process.

5. CONCLUSIONS

1. The research proves that stability and high quality operations of the technological processes with randomly variable perturbations (wastewater biological cleaning, steam production, etc.) can be realised using invariant control system with major disturbance impact preemptive compensation on control object output parameters.

2. A steam boiler invariant PID-DPC control system with disturbances preemptive compensation controller, the algorithm and parameters of which are correctly compiled according to the invariant control principle, cancels out the impact of main external disturbances – the fluctuating steam expenditure $q_s(t)$ and the feed water flow changes $q_w(t)$ on the steam boiler output variable – steam pressure $p(t)$.

3. Simulations show that for steam boiler feedback control system with only PID controller and optimally tuned parameters the maximum deviation of the control variable – steam pressure $p(t)$ is up to 50 % under linear growing rate of steam expenditure from no-load to rated value, showing overall unacceptable control quality and inability to compensate fast variable disturbances.

4. Simulation results make possible to forecast that introducing in practice the invariant PID-DPC control system with disturbances $q_s(t)$ and $q_w(t)$ preemptive compensation controller, the fluctuations of boiler steam pressure $p(t)$ do not exceed ± 3 % of rated value because of high sensitivity of disturbance controller and high-speed response of systems actuator to disturbances.

5. The developed methodology of invariant control system modelling and design for wastewater aeration and water steam production plants can be successfully applied to other technological processes and plants to be characterised by high influence of organised and randomly varying disturbances.

REFERENCES

1. Sniders, A., and Laizans, A. (2006). Invariant control of wastewater aeration. *Advances in Computer, Information, and Systems Sciences, and Engineering*, Univ. of Bridgeport, Inst. of Electrical and Electronics Eng. (IEEE), Bridgeport, USA: Springer, 99–103.
2. Laizans, A., and Sniders, A. (2008). Simulation of cost-efficient wastewater aeration control using invariant control Principle. *Sc. J. Agriculture and Engineering Complying with the European Requirements*, Bucharest, Romania, INMATEH Magazine, 24(I), 183–187.

3. Sniders, A., Laizans, A. (2007). Computer aided modelling of wastewater aeration. In *Conf. Proc. Rural Development 2007*, 8–10 November 2007. (pp. 227–231) 3 (2), Kaunas, Lithuania: Lith. Univ. of Agric.
4. Sniders, A., and Laizans, A. (2011). Adaptive model of wastewater aeration tank. *Sc. J. of Riga Tech. Univ. Environmental and Climate Technologies*. (13) 6, 112–117.
5. Qinling, Z., Zhiqiang, G., and Wen, T. (2011). Disturbance rejection in thermal power plants. In *30th Chinese Control Conference*, 22–24 July, (pp. 6350–6355), Yantai, China.
6. Ivezic, D., and Petrovic, T. (2010). Robust IMC controllers with optimal set-points tracking and disturbance rejection for industrial boiler. *J. Mechanical Engineering*, vol. 56, (565–574).
7. Sniders, A., and Rungulis, D. (2001). Adaptive control of the steam boiler for process needs in food production plant. Sc. *J. Industrial Heat Engineering, National Academy of Sciences, Ukraine*. 23 (3), 89–95. (In Russian).
8. Sniders, A. (2003). Transient process stabilization in a steam boiler. *Sc. J. of Riga Tech. Univ. Power and Electrical Engineering*, 4 (9), 166–171, ISSN 1407-7345. (In Latvian).
9. Henzinger, A., and Wong-Toi, H. (1996). *Using HYTECH to Synthesize Control Parameters for Steam Boiler. Lecture Notes in Computer Science*, University of California, Berkeley: Springer-Verlag.
10. Navritil, A., Pekar, L., and Masaryka, T.G. (2011). Possible solution of decoupling and invariance of multi-variable control loop by using correction members. *WSEAS Transactions on Circuits and Systems*, 6 (10), 209–219.
11. Sniders, A., and Komass, T. (2012). Invariant method of load independent pressure control in steam boiler. *Sc. J. of Riga Tech. U. Electrical, Control and Communication Engineering.* 1 (1), 5–10.
12. Sniders, A. (2010). Adaptive self-tuning model for non-stationary process simulation. In *Conf. Proc. Engineering for Rural Development 2010*, 27–28 May 2010 (pp.192–199) Vol. 9, Jelgava, Latvia: LUA, Fac. of Engineering.

TEHNOLOĢISKO IEKĀRTU INVARIANTA VADĪBA GALVENO PERTURBĀCIJU IESPAIDA APSTEIDZOŠAI KOMPENSĀCIJAI

A. Šnīders, A. Laizāns, T. Komass

K o p s a v i l k u m s

Rakstā piedāvāts pārskats par pētījumu rezultātiem, kas apliecina invariantās vadības metodes priekšrocības tehnoloģisko iekārtu, uz kurām iedarbojas būtiskas organizētas un stohastiskas perturbācijas kā, piemēram, notekūdeņu bioloģiskās attīrīšanas aerotenki un tvaika katli pārtikas produktu apstrādei ar tvaiku, darbības procesu vadības kvalitātes un energoefektivitātes uzlabošanai. Kā specifisks izpētes objekts apskatīts tvaika katla daudz-kontūru invariantās vadības sistēmas simulācijas modelis MATLAB/SIMULINK vidē. Sistēma sastāv no slēgtas cilpas vadības kontūra ar tradicionālo PID kontrolleri un tvaika spiediena mērīšanas pārveidotāju atgriezeniskajā saitē, un perturbāciju (tvaika patēriņa slodzes un pievadītā ūdens plūsmas) iespaida apsteidzošas kompensācijas vaļējas cilpas kontūriem ar divkanālu

kontrolleri DPC, kurš apsteidzoši aktivizē tvaika katla enerģētisko iekārtu, tiklīdz mainās kāda no perturbācijām, un tādā veidā savlaicīgi novērš spiediena izmaiņu tvaika katlā. PID kontrolleris reaģē uz perturbācijām novēloti, pēc tam kad vadības objektā jau notikušas būtiskas izmaiņas, un bez DPC kontrollera atbalsta nespēj nodrošināt atbilstošu tvaika spiediena stabilitāti pie straujas tvaika patēriņa izmaiņas. DPC kontrollera darbības algoritmi sastādīti atbilstoši invariances prasībām ciešā korelācijā ar vadības objekta un enerģētiskās izpildiekārtas darbības algoritmiem, to jutības un reakcijas laika parametriem. Simulācijas rezultāti apliecina, ka pateicoties DPC kontrollera adekvātai reakcijai gan uz organizētām, gan stohastiskām perturbācijām, to iespaids uz vadības objekta stabilizējamo izejas parametru tiek savlaicīgi kompensēts ar enerģētiskās iekārtas apsteidzošu, paātrinātu ierosināšanu, apejot galveno PID vadības kontūru.

11.05.2016.

LATVIAN JOURNAL OF PHYSICS AND TECHNICAL SCIENCES
2016, N 3
DOI: 10.1515/lpts-2016-0020

INFLUENCE OF VOLTAGE DIPS ON THE OPERATION OF BRUSHLESS EXCITER SYSTEM OF SYNCHRONOUS MACHINES

A. Fedotov[1], A. Leonov[1], G. Vagapov[1], A. Mutule[2]

[1] Kazan State Powering Engineering University
51 Krasnoselskaya Str., Kazan, RUSSIA
[2] Institute of Physical Energetics, 21 Aizkraukles Str., Riga, LV-1006, LATVIA

This paper presents a mathematical model with continuous variables for brushless exciter system of synchronous machines, containing the thyristor elements. Discrete Laplace transform is used for transition from a mathematical model of a system with variable structure in continuous variables to equation finite difference with permanent structure. Then inverse transition is made to a mathematical model in continuous variables with permanent structure.

Keywords: *discrete transformation, exciter system, mathematical model, semiconductor thyristor, synchronous motor.*

1. INTRODUCTION

This paper covers some issues of the development of a mathematical model of the synchronous machine in continuous variables taking into account the work of thyristor elements in exciter and ensuring adequate representation of electromagnetic processes based on the methods of converting the system from variable structure to permanent structure presented in various applications to electromechanical systems in [3]–[9].

Usually modern synchronous machines (SMs) are equipped with brushless exciter systems. They can be generators, as well as motors providing operation of respective technological mechanisms in the industrial plants of petrochemical complex, steel industry, in the system of thermal power plants for own needs. Short faults in distribution electrical networks of 110–220 kV cause voltage dips on sections 6–10 kV of distribution switchgear of substations, to which SMs are connected [1] in the distribution grids of 110–220 kV. Exciter system of SMs is powered through transformers from the same sections, which reduces their ability to the field forcing and it can lead to loss of synchronism and disconnection by the relay protection from the grid. It is necessary to have the appropriate mathematical model in order to assess stability reserve of SM depending on the depth of voltage dips. The problem of the exciter system includes thyristor elements: controlled (static exciter) and uncontrolled (rotating exciter) thyristors, conditional on variable structure of differential

equations, describe electromagnetic transient processes in SM [2]. In this case, any criteria estimation of stability reserve SM does not apply during short interruption of power supply (SIPS).

2. MATERIALS AND METHODS

2.1. Mathematical Model of SM with Variable Structure

A circuit diagram of the exciter system of SM is shown in Fig. 1, where VD1 – the controlled rectifier pre exciter, VD2 – the uncontrolled rectifier of exciter, located on the rotor of SM; resistance R1, R2, R3 and thyristors T1, T2 provide field discharge in emergency modes of SM. The switch Q is used to protect the SM and delivers its connection to the electricity grid.

The following assumptions are accepted for developing the mathematical model: the original equations of SM base on Park-Gorev model [10] with equivalenting damper contours of one winding longitudinal axis and one winding in the transverse axis, axis d outstrips axis q.

Assembled on the three-phase bridge configuration thyristors of managed converter are considered to be ideal and they operate in the native mode. Native mode is mode with alternate conduction of two and three thyristors. Angle α of natural opening of thyristors is calculated from zero of corresponding phase EMF. Generally accepted notation [10] is saved in equations of synchronous machine. "Step" system of coordinates is used taking into account the work of thyristors. Thyristors of both converters are considered operational simultaneously (simultaneous opening of appropriate thyristors), taking into account that angle α_0 of natural opening of thyristors depends on the phase of the EMF of grid 0.4 kV. The superscript "g" in the notation is used for parameters of exciter. Park–Gorev equation for SM will have the form:

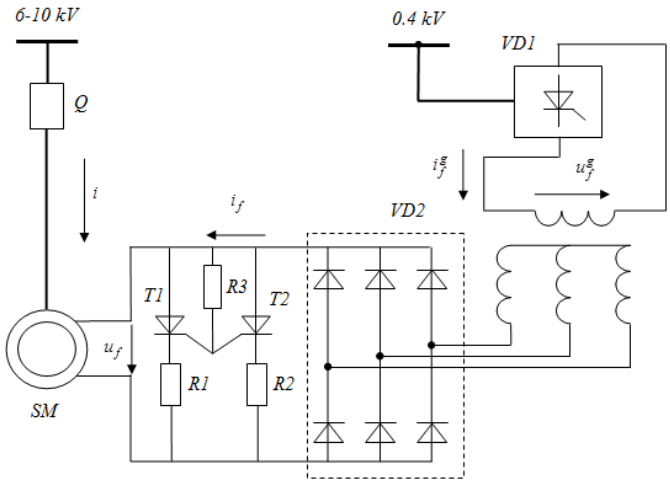

Fig. 1. Schematic diagram of the brushless exciter synchronous machine.

$$\left.\begin{aligned}
-u_d &= ri_d + \frac{d\Psi_d}{d\theta_c} + \omega\Psi_q, \quad \Psi_d = x_d i_d + x_{ad} i_f + x_{ad} i_{1d},\\
-u_q &= ri_q + \frac{d\Psi_q}{d\theta_c} - \omega\Psi_d, \quad \Psi_q = x_q i_q + x_{aq} i_{1q},\\
u_f &= r_f i_f + \frac{d\Psi_f}{d\theta_c}, \quad \Psi_f = x_{ad} i_d + x_f i_f + x_{ad} i_{1d},\\
0 &= r_{1d} i_{1d} + \frac{d\Psi_{1d}}{d\theta_c}, \quad \Psi_{1d} = x_{ad} i_d + x_{ad} i_f + x_{1d} i_{1d},\\
0 &= r_{1q} i_{1q} + \frac{d\Psi_{1q}}{d\theta_c}, \quad \Psi_{1q} = x_{aq} i_q + x_{1q} i_{1q}.
\end{aligned}\right\} \tag{1}$$

Differential equation exciter will have the form:

$$\left.\begin{aligned}
-u_d^g &= r^g i_d^g + \frac{d\Psi_d^g}{d\theta_c} + \omega\Psi_q^g, \quad \Psi_d^g = x_d^g i_d^g + x_{ad}^g i_f^g + x_{ad}^g i_{1d}^g,\\
-u_q^g &= r^g i_q^g + \frac{d\Psi_q^g}{d\theta_c} - \omega\Psi_d^g, \quad \Psi_q^g = x_q^g i_q^g + x_{aq}^g i_{1q}^g,\\
u_f^g &= r_f^g i_f^g + \frac{d\Psi_f^g}{d\theta_c}, \quad \Psi_f^g = x_{ad}^g i_d^g + x_f^g i_f^g + x_{ad}^g i_{1d}^g,\\
0 &= r_{1d}^g i_{1d}^g + \frac{d\Psi_{1d}^g}{d\theta_c}, \quad \Psi_{1d}^g = x_{ad}^g i_d^g + x_{ad}^g i_f^g + x_{1d}^g i_{1d}^g,\\
0 &= r_{1d}^g i_{1d}^g + \frac{d\Psi_{1d}^g}{d\theta_c}, \quad \Psi_{1q}^g = x_{aq}^g i_q^g + x_{1q}^g i_{1q}^g.
\end{aligned}\right\} \tag{2}$$

We write the equation of the relation between the excitation winding and exciter SM. For this equation of voltage balance for the excitation circuit of synchronous motor at the side of the exciter, local transformation on the m-recurrence interval is used. We consider one recurrence interval converter, including switching interval. The following voltage balance equation is valid in the stepping coordinate system, associated with switching thyristors, inside the recurrence interval converter within the length of phase commutation γ.

$$-\sqrt{3}u_d^{g(m)} \sin\left(\theta^{(m)} - \pi/3\right) + \sqrt{3}u_q^{g(m)} \cos\left(\theta^{(m)} - \pi/3\right) = u_f^{(m)}. \tag{3}$$

It will be equation considering the first two systems of equations (2) and the third equation of (1).

$$\frac{d}{d\theta}\left[\psi_f^{(m)} - \sqrt{3}\psi_d^{g(m)}\sin\left(\theta^{(m)} - \pi/3\right) + \sqrt{3}\psi_q^{g(m)}\cos\left(\theta^{(m)} - \pi/3\right)\right] =$$
$$= \sqrt{3}r^g\left[i_d^{g(m)}\sin\left(\theta^{(m)} - \pi/3\right) - i_q^{g(m)}\cos\left(\theta^{(m)} - \pi/3\right)\right] - r_f i_f^{(m)}. \quad (4)$$

The following relations link currents with each other

$$\left.\begin{aligned}
&i_d^{g(m)} = \left(-2/\sqrt{3}\right)\left[i_f^{(m)}\sin\left(\theta^{(m)} - \pi/3\right) + i_\gamma^{(m)}\sin\left(\theta^{(m)} + \pi/3\right)\right],\\
&i_q^{g(m)} = \left(2/\sqrt{3}\right)\left[i_f^{(m)}\cos\left(\theta^{(m)} - \pi/3\right) + i_\gamma^{(m)}\cos\left(\theta^{(m)} + \pi/3\right)\right],\\
&\theta^{(m)} \in [\alpha_0^{(m)};\quad \alpha_0^{(m)} + \gamma_0^{(m)}];\\
&i_d^{g(m)} = \left(-2/\sqrt{3}\right) i_f^{(m)}\sin\left(\theta^{(m)} - \pi/3\right),\\
&i_q^{g(m)} = \left(2/\sqrt{3}\right) i_f^{(m)}\cos\left(\theta^{(m)} - \pi/3\right),\\
&\theta^{(m)} \in [\alpha_0^{(m)} + \gamma_0^{(m)};\quad \alpha_0^{(m)} + \pi/3].
\end{aligned}\right\} \quad (5)$$

Wherein

$$i_\gamma^{(m)}\left(\alpha_0^{(m)}\right) = i_f^{(m)}\left(\alpha_0^{(m)}\right),\quad i_\gamma^{(m)}\left(\alpha_0^{(m)} + \gamma_0^{(m)}\right) = 0,$$

where α_0 – the angle of control of converter *VD*2 (Fig. 1).

The following equation is also true in the switching interval obtained based on balance voltage in the switching circuit:

$$\sqrt{3}u_d^{g(m)}\sin\left(\theta^{(m)} + \pi/3\right) - \sqrt{3}u_q^{g(m)}\cos\left(\theta^{(m)} + \pi/3\right) = 0.$$

It takes the following form after substituting voltage from (3)

$$\frac{d}{d\theta}\left[\sqrt{3}\psi_d^{g(m)}\sin\left(\theta^{(m)} + \pi/3\right) - \sqrt{3}\psi_q^{g(m)}\cos\left(\theta^{(m)} + \pi/3\right)\right] =$$
$$= -\sqrt{3}r^g\left[i_d^{g(m)}\sin\left(\theta^{(m)} + \pi/3\right) - i_q^{g(m)}\cos\left(\theta^{(m)} + \pi/3\right)\right]. \quad (6)$$

We introduce the following notation for the flux linkage:

$$\psi_{fg}^{(m)} = x_{ad}i_d^{(m)} + \left[x_f + x_d^g + x_q^g - \left(x_d^g - x_q^g\right)\cos 2\left(\theta^{(m)} - \pi/3\right)\right] i_f^{(m)} -$$
$$- \sqrt{3}x_{ad}^g\sin\left(\theta^{(m)} - \pi/3\right) i_f^{g(m)} - \sqrt{3}x_{ad}^g\sin\left(\theta^{(m)} - \pi/3\right) i_{1d}^{g(m)} +$$
$$+ \sqrt{3}x_{aq}^g\cos\left(\theta^{(m)} - \pi/3\right) i_{1q}^{g(m)} - \left[\frac{x_d^g + x_q^g}{2} + \left(x_d^g - x_q^g\right)\cos 2\theta^{(m)}\right] i_\gamma^{g(m)};$$

$$\psi_f^{g(m)} = -\frac{2}{\sqrt{3}} x_{ad}^g \sin\left(\theta^{(m)} - \pi/3\right) i_f^{(m)} + x_f^g i_f^{g(m)} + x_{ad}^g i_{1d}^{g(m)} - \frac{2}{\sqrt{3}} x_{ad}^g \sin\left(\theta^{(m)} + \pi/3\right) i_\gamma^{(m)};$$

$$\psi_{f\gamma}^{(m)} = \left[\frac{x_d^g + x_q^g}{2} + \left(x_d^g - x_q^g\right)\cos 2\theta^{(m)}\right] i_f^{(m)} + \sqrt{3} x_{ad}^g \sin\left(\theta^{(m)} + \pi/3\right) i_f^{g(m)} -$$
$$- \sqrt{3} x_{ad}^g \sin\left(\theta^{(m)} + \pi/3\right) i_{1d}^{g(m)} - \sqrt{3} x_{aq}^g \cos\left(\theta^{(m)} + \pi/3\right) i_{1q}^{g(m)} -$$
$$- \left[x_d^g + x_q^g - \left(x_d^g - x_q^g\right)\cos 2\left(\theta^{(m)} + \pi/3\right)\right] i_\gamma^{(m)}.$$

The obtained expressions allow writing differential equation concerning the flux linkage using (5) and (6):

$$\left.\begin{aligned}
\frac{d\psi_d^{(m)}}{d\theta_c} &= ri_d^{(m)} \quad \omega\psi_q^{(m)} \quad u_d^{(m)};\\
\frac{d\psi_q^{(m)}}{d\theta_c} &= ri_q^{(m)} + \omega\psi_d^{(m)} \quad u_q^{(m)};\\
\frac{d\psi_{fg}^{(m)}}{d\theta_c} &= \left(r_f + 2r_g\right) i_f^{(m)} + r_g i_\gamma^{(m)},\\
& \quad i_\gamma^{(m)} \equiv 0 \;\; with \;\; \theta \in \left[\alpha_0^{(m)} + \gamma_0^{(m)}; \alpha_0^{(m)} + h^{(m)}\right];\\
\frac{d\psi_{f\gamma}^{(m)}}{d\theta_c} &= r_g i_f^{(m)} + 2r_g i_\gamma^{(m)},\\
& \quad \theta \in \left[\alpha^{(m)}; \alpha^{(m)} + \gamma^{(m)}\right];\\
\frac{d\psi_{1d}^{(m)}}{d\theta_c} &= r_{1d} i_{1d}^{(m)};\\
\frac{d\psi_{1q}^{(m)}}{d\theta_c} &= r_{1q} i_{1q}^{(m)};\\
\frac{d\psi_f^{g(m)}}{d\theta_c} &= r_f^g i_f^{g(m)} + u_f^{g(m)};\\
\frac{d\psi_{1d}^{g(m)}}{d\theta_c} &= r_{1d}^g i_{1d}^{g(m)};\\
\frac{d\psi_{1q}^{g(m)}}{d\theta_c} &= r_{1q}^g i_{1q}^{g(m)}.
\end{aligned}\right\} \qquad (7)$$

The voltage u_f^g of exciter is not determined in (7). The voltages u_d and u_q are determined after writing the equations of electric grid external to SM.

2.2. The Dynamic Characteristics of the External Converter Pre-exciter

Voltage balance equation will be the following for single-phase thyristor converter VD1 (Fig. 1), in the transition process [2], [7], [9] in the range of its repeat-

ability

$$u_f^g = u_c(\theta) - r_c i_f^g - x_c \frac{di_f^g}{d\theta} - K(\theta)\left(r_c i_\gamma^g - x_c \frac{di_\gamma^g}{d\theta}\right), \tag{7a}$$

where u_c – the mains voltage, power supply converter pre-exciter;

r_c and x_c – active and inductive resistance of power supply converter pre-exciter, respectively;

i_γ^g – switching current, wherein $i_\gamma^g(\alpha) = -2i_f^g(\alpha)$, $i_\gamma^g(\alpha+\gamma) = 0$;

$K(\theta) = 1(\theta - \alpha) - 1(\theta - \alpha - \gamma)$ – a key step function;

$1(\theta - \alpha)$, $1(\theta - \alpha - \gamma)$ – a single function.

According to [11], local integral transformation (LIT) function $f(\theta)$ on т- th interval discretization $[\alpha \quad \alpha + h^{(m)}]$ is determined in the following way

$$F(m) = \frac{1}{h^{(m)}} \int_{\alpha + h^{(m)}}^{\alpha} f(\theta) d\theta \tag{8}$$

According to (8), LIT collates the continuous function of its discrete average value at a predetermined interval.

If in the grid of 0.4 kV the supply voltage of converter does not change in the transitional process on the side of a high voltage, it can be taken as $u_c(\theta) = E_c \sin\theta$. Applying LIT for (7) on the *m*-th interval of borders $[\alpha \quad \alpha + \pi]$, we obtain

$$U_{fs}^{g(m)} = \frac{2E_c}{\pi}\cos\alpha - r_c I_{fs}^{g(m)} - \left(\frac{2x_c}{\pi} - \frac{r_c\gamma}{\pi}\right) i_{fl}^{g(m)} - \frac{x_c}{\pi}\Delta i_{fl}^{g(m)}. \tag{9}$$

In (9) subscript "*s*" means the average value of a variable interval of discretization, subscript "*l*" applies to the value of the variable at the starting point of the interval.

It can be written using a linear approximation of the current

$$i_{fl}^{g(m)} \approx i_{fs}^{g(m)} - \frac{1}{2}\Delta i_{fl}^{g(m)}. \tag{10}$$

The dynamic external characteristic of converter in discrete variables is obtained after substituting (10) in (9):

$$U_f^{g(m)} = \frac{2E_c}{\pi}\cos\alpha - \left(r_c + \frac{2x_c}{\pi} - \frac{r_c\gamma}{\pi}\right) I_{fs}^{g(m)} - \frac{r_c\gamma}{2\pi}\Delta i_{fl}^{g(m)}. \tag{11}$$

Active resistance r_c is much less compared with inductive impedance of $\tilde{o}_{\tilde{n}}$ converter transformer of pre-exciter connected to 0.4 kV. We neglect its influence in (11). Then it conclusively turns into

$$U_f^{g(m)} = \frac{2E_c}{\pi}\cos\alpha - \frac{2x_c}{\pi} I_{fs}^{g(m)}.$$

Corresponding to the equivalent, the equation can be written in the instantaneous values of variables

$$u_f^g = \frac{2E_c}{\pi}\cos\alpha - \frac{2x_c}{\pi} i_f^g. \tag{12}$$

Control angle α is measured from zero phase EMF on the side of 0.4 kV in (12).

Appropriate voltage dip arises on the side of 0.4 kV during voltage dips on the side of 6–10 kV. In this case, supply voltage of excitation winding of exciter invariable should not be considered. It is possible to take [10], according to which supply voltage of converter of pre-exciter is expressed by the following equation

$$u_c(\theta) = U_{cp}\sin(\theta - \psi_p) + (U_{c0} + U_{cp}\sin\psi_p)e^{-\chi\theta}, \tag{13}$$

where $ctg\psi_p = \chi = 1/\omega T_p$, T_p – time constant in the transitional process, U_{c0} – initial voltage of dip; U_{cp} – the final voltage of dip (at $\theta \to \infty$).

It is necessary to determine the limit of integration interval for the use of LIT. Since they are combined with recurrence intervals of converter, their duration is unequal. The second term of (13) influences the duration of each interval.

Part of the voltage waveform is below abscissa axis even at $\theta > 0$ under ordinary proportions of grid settings:

$$\begin{aligned} U_{cs}^{(m)} &= \frac{1}{2\pi}\int_{\alpha_1+2\pi m-\psi_p}^{\alpha_2+2\pi m-\psi_p} u_c(\theta)d\theta - \frac{1}{2\pi}\int_{\alpha_2+2\pi m-\psi_p}^{\alpha_1+2\pi(m+1)-\psi_p} u_c(\theta)d\theta = \\ &= \frac{1}{\pi}U_{cp}[\cos(\alpha_1) - \cos(\alpha_2)] + \frac{1}{2\pi\chi}U_a\left[e^{-\chi\alpha_1}(1 + e^{-\chi 2\pi}) - 2e^{-\chi\alpha_2}\right]e^{-\chi(2\pi m-\psi_p)}. \end{aligned} \tag{14}$$

Equation (14) defines the law of change of the voltage to the exciter winding in the case of disturbance on the grid side. It contains the angle values α_1 and α_2, determining the interval of operating time cathode group of thyristors of converter *VD*1 (Fig. 1). The necessary changes should be performed to exclude these angles from (14). Attenuation of the aperiodic component will not be taken into account in (13):

$$u_c = A\sin(\theta - \alpha) + B\ . \tag{15}$$

Then the beginning of positive half of waves of the rectified voltage corresponds to the implementation of conditions

$$\sin\alpha = B / A\,. \tag{16}$$

Apparently, process is periodic with period 2π that is described by (15). It is also obvious that the duration of the anode T_1 and that of cathode T_2 half-wave rectified voltage are not the same, moreover $T_1 = \pi+2\alpha$, $T_2 = \pi-2\alpha$.

Value of average rectified voltage on m-th interval of periodicity:

$$U_s(m) = \frac{2}{\pi} A\cos\alpha + \frac{2}{\pi} B(m)\alpha\,. \tag{17}$$

Equation (17) shows that taking into account the unequal duration of each half-wave rectified voltage resulted, at first, in the appearance of the second term in the equation, associated with the aperiodic component of supply voltage. Secondly, the first term in (17) also becomes dependent on the number of considered intervals, because angle α changes from interval to interval, decreasing to zero in the steady mode at fully open thyristors.

From (16) the following equation is written:

$$\cos\alpha(m) = \sqrt{1-\sin^2\alpha(m)} = \sqrt{1-\left[B(m)/A\right]^2}\,.$$

It can be written taking into account attenuation of the aperiodic component of voltage

$$\cos\alpha(m) = \sqrt{1-\left(Be^{-\chi 2\pi(m-1)}/A\right)^2} \approx 1-\frac{1}{2}\left(Be^{-\chi 2\pi(m-1)}/A\right)^2. \tag{18}$$

Equation (16) is also transformed in the following way:

$$\sin\theta = Be^{-\chi[\theta+2\pi(m-1)]}/A\,. \tag{19}$$

Calculations show that switching of thyristors takes place near the point of their opening in the steady mode near the value $\theta = 0$. In this case:

$$\sin\theta \approx \theta,\ e^{-\chi[\theta+2\pi(m-1)]} \approx e^{-\chi 2\pi(m-1)} + \frac{d}{d\theta} f(\theta)\Big|_{\theta=0} {}^*\theta = e^{-\chi 2\pi(m-1)}(1-\chi\theta). \tag{20}$$

The next step is the change in equation (19) of relevant functions of their approximations by (29)

$$\alpha = \frac{e^{-\chi 2\pi(m-1)}}{1+\chi e^{-\chi 2\pi(m-1)}}\,. \tag{21}$$

Therefore, taking into account (18) and (21), we obtain the following law of changes of average rectified voltage for *m*-th range of full repeatability of converter circuit

$$U_s(m) = \frac{2}{\pi}\left[A - \frac{B^2}{2A}e^{-\chi 4\pi(m-1)}\right] + \frac{2}{\pi}B\frac{e^{-\chi 4\pi(m-1)}}{1+\chi e^{-\chi 2\pi(m-1)}}. \tag{22}$$

We have the following equation after transition from discrete variables (22) to continuous

$$u_s(\theta) = \frac{2}{\pi}\left[A - \frac{B^2}{2A}e^{-\chi 2\theta}\right] + \frac{2}{\pi}B\frac{e^{-\chi 4\theta}}{1+\chi e^{-\chi 2\theta}}. \tag{23}$$

Discrete variables are used for calculation of transient electromagnetic processes because the obtained finite-difference equations are best suited for their numerical solution. In those cases when electromechanical transition processes are considered, which are accompanied by changes in the speed of synchronous motors, differential equations of continuous variables become more comfortable. In the first case, it is advisable to use (22), and in the second case – (23).

2.3. Mathematical Model of the Exciter

Differential equations (7) have a variable structure. Their type and quantity depend on the number of conductive thyristors of converter pre-exciter and exciter. Using LIT allows obtaining equations with permanent structure. Therefore, we use (8) for the third equation of system (7) assuming that $h^{(m)} = \pi/3, \theta \in [\alpha_0\ \alpha_0 + \pi/3]$. Let us take linear approximation of the current switching $i_\gamma^{(m)}(\theta)$ on the integration interval $\theta \in [\alpha_0\ \alpha_0 + \gamma]$. The duration of the intervals $h^{(m)}$ of the constancy of the structure converter *VD*2 in the transition process and the switching angle γ will change. Numerical calculations of transient processes in the electric machine-thyristor motors show [2]–[7] that these factors can be ignored and take their steady-mode values.

The result is

$$\begin{aligned}
&x_{ad}\frac{\Delta i_d^{(m)}}{\pi/3} + \left[x_f + x_d^g + x_q^g - \left(x_d^g - x_q^g\right)\cos 2\alpha_0\right]\frac{\Delta i_f^{(m)}}{\pi/3} + x_{ad}\frac{\Delta i_{1d}^{(m)}}{\pi/3} + \left[\frac{x_d^g + x_q^g}{2\pi/3} - \frac{r_g\gamma}{2\pi/3} + \right.\\
&\left. + \frac{\sqrt{3}}{\pi/3}\left(x_d^g - x_q^g\right)\sin\left(2\alpha_0 - \pi/6\right)\right] i_{fl}^{(m)} - \sqrt{3}x_{ad}^g\sin\alpha_0\frac{\Delta i_f^{g(m)}}{\pi/3} - \frac{\sqrt{3}x_{ad}^g}{\pi/3}\cos\left(\alpha_0 - \pi/6\right) i_{fl}^{g(m)} -\\
&- \sqrt{3}x_{ad}^g\sin\alpha_0\frac{\Delta i_{1d}^{g(m)}}{\pi/3} - \frac{\sqrt{3}x_{ad}^g}{\pi/3}\cos\left(\alpha_0 - \pi/6\right) i_{1dl}^{g(m)} + \sqrt{3}x_{aq}^g\cos\alpha_0\frac{\Delta i_{1q}^{g(m)}}{\pi/3} -\\
&- \frac{\sqrt{3}x_{aq}^g}{\pi/3}\sin\left(\alpha_0 - \pi/6\right) i_{1q}^{g(m)} + \left(r_f + 2r_g\right) i_{fs}^{(m)} = 0.
\end{aligned} \tag{24}$$

It is acceptable to use $x_d^g \approx x_q^g$ for synchronous motors with brushless excitation system. It is possible to ignore the influence of snubber contours with time constant of transient processes also for engines with power several megawatts. As a result, it is possible to reduce (26) to the next taking into account the ratios of the parameters:

$$x_{ad}\frac{\Delta i_d^{(m)}}{\pi/3}+x_f\frac{\Delta i_f^{(m)}}{\pi/3}+\frac{x_d^g}{\pi/3}i_{fl}^{(m)}-\sqrt{3}x_{ad}^g\sin\alpha_0\frac{\Delta i_f^{g(m)}}{\pi/3}-$$
$$-\frac{\sqrt{3}x_{ad}^g}{\pi/3}\cos(\alpha_0-\pi/6)i_{fl}^{g(m)}+\left(r_f+2r_g\right)i_{fs}^{(m)}=0. \qquad (25)$$

Equation (25) cannot be attributed either to finite-difference equations, because it contains the average value of the variable $i_{fs}^{(m)}$, or to the equations in jaggies [11], because it contains samples of variables $i_{fl}^{(m)}$ and $i_{fl}^{g(m)}$. Therefore, (25) is necessary to lead to the first or another type. The value of (25) is in permanent structure and it does not depend on the switching thyristor inside the discretization interval. As excitation currents of pre-exciter and exciter, accordingly $i_{fl}^{(m)}$ and $i_{fl}^{g(m)}$, are smoothed by large inductance of the windings, let us assume that, $i_{fl}^{(m)} \approx i_{fs}^{(m)}$ and $i_{fl}^{g(m)} \approx i_{fs}^{g(m)}$. Then, according to [11], the resulting equation in the jaggies will correspond to the following equivalent differential equation in the continuous variables

$$x_{ad}\frac{di_d}{d\theta}+x_f\frac{di_f}{d\theta}-\sqrt{3}x_{ad}^g\sin\alpha_0\frac{di_f^g}{d\theta_c}-\frac{\sqrt{3}x_{ad}^g}{\pi/3}\cos(\alpha_0-\pi/6)i_f^g+\left(r_f+2r_g+\frac{x_d^g}{\pi/3}\right)i_f=0. \qquad (26)$$

Active resistance compared with inductive resistance of rotor of pre-exciter can be ignored in the last term of (28), if only active resistance in the rotor circuit is not entered to decrease the field.

Differential equation of pre-exciter needs to be added for obtained equations. It looks like written relatively discrete variables

$$U_{fs}^{g(m)}=r_f^g i_{fs}^{g(m)}-\frac{2\sqrt{3}}{\pi}x_{ad}^g\sin\alpha\Delta i_f^{(m)}+x_f^g\frac{\Delta i_f^{g(m)}}{\pi/3}. \qquad (27)$$

The equivalent differential equation correspondence:

$$u_f^g=r_f^g i_f^g-\frac{2\sqrt{3}}{3}x_{ad}^g\sin\alpha\frac{di_f}{d\theta}+x_f^g\frac{di_f^g}{d\theta}. \qquad (28)$$

Equation (28) should be used simultaneously with (23) because $u_f^g = u_s(\theta)$

3. RESULTS AND DISCUSSION

Usually switchgear section of power plants and substations of 110–220 kV are electrically connected through sectional switches. In these cases, short circuits spread in grids of 110–220 kV as voltage dips and for low voltage levels of connected substations. As a result, automatic reserve switching becomes ineffective and exciters of synchronous machines work at low voltage. The law of this change is determined by the parameters of the external power supply system.

The resulting mathematical model of brushless excitation system, containing two thyristor converters, allows performing calculations of verification of working modes of SM under conditions of influence of short-term power outages on the system of excitation through the supply grids.

Voltage dips with rectangular shape cause simultaneous reduction of excitation current of pre-exciter and SM. Aperiodic character of the voltage changes at short-term power may cause short rise of the excitation current of pre-exciter.

The laws of change excitation current of synchronous motors on the initial parts depend on shape of the curve voltage dip: the aperiodic law of changes in supply voltage causes the growth of the excitation current at the beginning of the transitional process.

Discrete mathematical model permanent structure of excitation system of SM adequately reproduces electromagnetic transient processes that allow using it for return to continuous variables. Switching current i_γ can be approximated in linear form during its integrating. It requires individual research for distribution of discrete models in electromechanical transient process, because changing of the rotational speed of SM is determined by changes in the electromagnetic moment, which cannot be converted mathematically rigorous to step images or finite difference sight. Having carried out a pre-removal switching of thyristors taking into consideration the method proposed above, it is recommended to remain in the framework of mathematical model in continuous variables.

4. CONCLUSIONS

A special feature of mathematical modelling of a synchronous machine with a brushless excitation system is needed for adequate mapping simultaneous operation of two converters, causing the variable structure of differential equations. This problem allows removing transition to equivalent equations. Intermediate transition from discrete variables to local image for each inverter followed by a return to differential equations with permanent structure provides a mathematical description of the synchronous motor operation with respect to “useful” components in the currents of excitation.

Short circuits in the external power supply system lead to voltage dips in both sections of low voltage in industrial substations, which makes inefficient the system of reservation power of excitation windings of synchronous machine exciter from adjacent sections of switchgears of the systems of internal power supply.

Perhaps the mathematical description of electromagnetic transients in syn-

chronous machines is appropriate in the form of finite-difference equations. The speed of calculations is repeatedly increased and conditions are created for the development of automatic systems of control and protection, using "the projected" development mode under external distortion. It is reasonable to use the mathematical model of a permanent structure in the continuous variables for the description of electromechanical transient process.

REFERENCES

1. Abdullazyanov, E.Y. (2009). Limiting the Impact of Short-Term Power Failure at Industrial Consumers. Scientific publication. Publishing House of KSPEU.
2. Kuznetsov, V.A., and Fedotov, A.I. (1999). Using the local Fourier transform for the mathematical modeling of synchronous machines with brushless excitation systems. *Electricity*. No. 4, 13–22.
3. Kryuchkov, I.P., Starshinov, V.A., and Gusev, Y.P. et al. (2008). *Transients in Electric Power Systems*. Moscow: Publishing House MEI.
4. Beregovenko, G.Y., Pukhov, G.E., and Saukh, S.E. (1993). *Numerical Methods for Solving Differential Operator Equations and Analysis of Dynamical Systems.* Kiev: Science. Dumka.
5. Zhenya, L. (2015). *Ultra-High Voltage AC/DC Grids*. Academic Press.
6. Huadong, S., Yong, T., and Shiying, M. (2006). A commentary on definition and classification of power system stability. *Power Syst. Technol.* 30(17), 31–35.
7. Xiaojiang, G., Yong, T., Qiang, G. et al. (2012). Influence factors and theory for CIGRE MSCR index. *Power Syst. Prot. Control.* 40(9), 69–74.
8. Xiaojiang, G., Jianbo, G., Shiying, M. et al. (2013). A method for multi DC terminal location selection based on multi-infeed short circuit ratio. *Proc. CSEE.* 33(10), 36–42.
9. Rongjiang, C., Nihong, G., and Yong, S. (1996). Test study on self-extinction behavior of secondary arc on power system. *Proc. CSEE.* 16(2), 73–78.
10. Curatolo T, and Cogger S. (2005). Enhancing a power supply to ensure EMI compliance. *EDN*. 50(2), 67–74.

SPRIEGUMA IETEKME UZ SINHRONO MAŠĪNU AR BEZSUKU IEROSMES SISTĒMU

Fedotovs A., Leonovs A. Vagapovs G., Mutule A.

K o p s a v i l k u m s

Rakstā piedāvāts matemātiskais modelis ar nepārtraukti mainīgajiem lielumiem sinhronai mašīnai ar bezsuku ierosmes sistēmu, saturošu tiristora elementu. Laplasa diskrētā transformācija tiek izmantota pārejai no vienādojumiem maināmai struktūrai ar nepārtraukti mainīgu lielumu matemātisko modeli uz galīgu diferenču vienādojumiem pastāvīgām struktūrām. Pēc tam veikta apgrieztā pāreja uz matemātisko modeli ar nepārtraukti mainīgiem lielumiem pastāvīgai struktūrai.

25.02.2016.

LATVIAN JOURNAL OF PHYSICS AND TECHNICAL SCIENCES
2016, N 3

DOI: 10.1515/lpts-2016-0021

SOLID STATE PHYSICS

PRODUCTION OF ZnO AND CdO-ZnO THIN FILMS BY EXTRACTION–PYROLYTIC METHOD

A. Cvetkovs[1], O. Kiselova[2], U. Rogulis[2], V. Serga[1], R. Ignatans[2]

[1]Institute of Inorganic Chemistry, Riga Technical University, 34 Miera Str., Salaspils, LV-2169, LATVIA
E-mail: antonzweig@hotmail.lv

[2]Institute of Solid State Physics, University of Latvia, 8 Kengaraga Str., LV-1063, LATVIA

The extraction-pyrolytic method has been applied to produce the ZnO and CdO-ZnO thin films on glass and quartz glass substrates. According to X-ray diffraction measurements, the ZnO and CdO phases have been produced with an average size of crystallites about 8–42 nm in the films. The thickness of the layers measured by a profilometer has been up to 150 nm. The surface morphology measurements show that the surface of the films may be rough and non-continuous. The SEM results confirm the dependence between the preparation procedure and the quality of the thin film.

Keywords: *CdO-ZnO thin films, extraction-pyrolytic method, surface morphology, X-ray diffraction.*

1. INTRODUCTION

Zinc oxide ZnO is an n-type semiconductor. Due to its crystalline structure parameters, wide band gap (approximately 3.7 eV at room temperature), high exciton bound energy (60 meV) and possibilities to embed several impurities, ZnO has good optical, electrical, piesoelectrical and magnetic properties [1]. The above-mentioned properties can be changed by adding appropriate amounts of impurities or by alloying ZnO with other materials. As an example, the band gap of the pure ZnO of 3.37 eV could be increased up to 7.8 eV by adding the MgO [2], or decreased to 2.3 eV by adding the CdO [3]. ZnO serves as important material with various applications in production of photodetectors, light diodes, biosensors, solar batteries, etc. [1], [4]–[8].

CdO-ZnO thin films can be produced by several known technologies, such as chemical vapour deposition, “sol-gel” technique, laser ablation, radio-frequency and DC magnetron sputtering methods [9]–[14]. Each method has advantages and disad-

vantages in terms of production procedures, equipment costs and resulting product properties; therefore, the development of new semiconductor production methods remains challenging.

The aim of the present research is to produce the thin films of CdO-ZnO by the extraction-pyrolytic method (EPM) [14]. Comparing with other production techniques of thin films the EPM has several advantages. In case of using the EPM vacuum or high pressure, high electrical and magnetic fields, low or high temperatures are not necessary. This technology is simple and corresponds to the ecological standards. In principle, the EPM allows varying and optimising the composition, structure and properties of composite materials [15].

2. EXPERIMENTAL PROCEDURE

In order to produce the thin layers of ZnO and CdO-ZnO, the cadmium and zinc extracts were prepared. Zinc and cadmium were extracted from chloride solutions by the caproic acid without use of organic solvents, previously adding the sodium hydroxide solution in stoichiometric proportions. In order to remove the sodium ions from the organic phase, the extracts were flushed 3 times with newly prepared zinc chloride or cadmium chloride solutions. The extraction of the metal cations occurs according to the cation exchange mechanism as shown by the following reaction:

$$Me^{n+}_{(w)} + nHR_{(o)} \rightarrow MeR_{n(o)} + nH^{+}_{(w)},$$

where w refers to the water phase and o – to the organic phase.

In order to determine the exact concentration of cadmium in the cadmium extract, in a platinum crucible appropriate volume of the extract was heated to 600 °C and held at this temperature for 30 minutes. The exact mass of the produced CdO and the concentration of the cadmium extract were calculated. The concentration of cadmium extract was found to be 0.31 mol/L.

In order to determine the exact concentration of zinc in the zinc extract, in a platinum crucible known volume of cadmium extract was added to an appropriate volume of zinc extract and the prepared mixture of extracts was heated to 600 °C (in muffle furnace SNOL 8,2/1100 L “UMEGA”) and kept at this temperature for 30 minutes. In parallel, the procedure was repeated with the mixture of known volume of cadmium acetate dihydrate solution in ethanol with known concentration and known volume of zinc extract. The ratio between zinc and cadmium in the produced samples was determined by using the EDAX Eagle III Micro-XRF elemental analyser. The found ratios were used to calculate the concentration of zinc extract. Two independent calculations of the concentration of zinc extract gave the same results. The concentration of zinc extract was found to be 0.048 mol/L.

In additional, the solution of the cadmium acetate in ethanol with a concentration of 0.048 mol/L was prepared. In order to produce thin films with different compositions, the prepared organic extracts and cadmium acetate solutions were mixed in different proportions. Extracts and their solutions were additionally diluted with caproic acid and ethanol. Defined volumes of prepared organic solutions were

applied on the glass or the quartz glass substrates. The substrates were previously treated by a 10 % NaOH solution, washed in hot water, dried and treated with dichloroethane in an ultrasonic bath. After the evaporation of the solvent, the samples were heated under constant heating rate ($v_{heat.}$) from room temperature to the thermal treatment temperature ($T_{ann.}$) and held at this temperature for a definite time ($t_{ann.}$). Before the thermal treatment at high temperatures, the samples were dried at room temperature. This cycle of the application of organic precursor and thermal treatment in air was repeated several times. The conditions of the process are shown in Table 1.

The XRD patterns were obtained by a PANalytical X'Pert PRO spectrometer at the wavelength of 1.542 Å (Cu K_α). In order to calculate the mean size of crystallites, preliminary processing of the resulting X-ray diffraction data was performed by using Origin software. For the determination of the size of crystallites (τ), the Scherrer equation was used:

$$\tau = \frac{K\lambda}{\beta \cos\theta},$$

where K is a dimensionless shape factor with a value of about 0.94, but varies with the actual shape of the crystallite; λ is the X-ray wavelength; β is the line broadening at half the maximum intensity (FWHM), after subtracting the instrumental line broadening, in radians, which was calculated by using peak shape approximation with the Pseudo-Voigt function; θ is the Bragg angle.

The thickness-profile measurements of the thin films were performed by a Vecco Dektak 150 Surface Profiler profilometer. The stylus radius was around 12.5 μm and the stylus force equalled 0.03–3 mg. The surface morphology of the thin films was evaluated by scanning electron microscopy (SEM). Secondary electrons and backscattered electrons were detected.

Table 1

Thin Film Preparation Conditions (I – Zinc Extract, II – Cadmium Extract, III – Cadmium Acetate in Ethanol)

Abbreviation of the thin film and its expected chemical composition	Type of used substrate and the covered area of substrate, cm^2	Total number of the application-thermal treatment cycles	Composition of the sublimated organic solution	Volume of the sublimated precursor solution, mL	Thermal treatment conditions
A* (ZnO)	Glass (19.5)	1	precursor I	0.82	1.$v_{heat.}$=7 °C/min, $T_{ann.}$=300 °C, $t_{ann.}$= 0 min 2. $T_{ann.}$=350 °C, $t_{ann.}$= 30 min
B (CdO·7ZnO)	Glass (19.5)	5	mixture of precursor I, precursor III and caproic acid in volume proportion of 1:0.147:1	0.16 (cycles 1-2) 0.32 (cycles 3-5)	$v_{heat.}$=15 °C/min (cycles 1–5), $T_{ann.}$=350 °C (cycles 1-4), $T_{ann.}$=400 °C (cycle 5), $t_{ann.}$=5 min (cycles 1-5)

C (CdO·7ZnO)	Quartz glass (19.6)	5	mixture of precursor I, precursor III and caproic acid in volume proportion of 1:0.147:1	0.16 (cycles 1-2) 0.32 (cycles 3-5)	$v_{heat.}$=15 ˚C/ min (cycles 1–5), $T_{ann.}$=350 °C (cycles 1-4), $T_{ann.}$=400 °C (cycle 5), $t_{ann.}$=5 min (cycles 1-5)
D (CdO·75ZnO)	Quartz glass (19.6)	8	mixture of precursor I, precursor III and caproic acid in volume proportion of 1:0.0133:1	0.15 (cycles 1-8)	$v_{heat.}$=15 ˚C/ min (cycles 1–8), $T_{ann.}$=350 °C (cycles 1-7), $T_{ann.}$=400 °C (cycle 8), $t_{ann.}$=5 min (cycles 1-7), $t_{ann.}$=30 min (cycle 8)
E (4CdO·7ZnO)	Quartz glass (19.6)	8	mixture of precursor I, precursor III and caproic acid in volume proportion of 1:0.57:1	0.19 (cycles 1-8)	$v_{heat.}$=15 ˚C/ min (cycles 1–8), $T_{ann.}$=350 °C (cycles 1-7), $T_{ann.}$=400 °C (cycle 8), $t_{ann.}$=5 min (cycles 1-7), $t_{ann.}$=60 min (cycle 8)
F (CdO)	Quartz glass (13.4)	8	mixture of precursor II and caproic acid in volume proportion of 1:5.25	0.10 (cycles 1-8)	$v_{heat.}$=15 ˚C/ min (cycles 1–8), $T_{ann.}$=350 °C (cycles 1-7), $T_{ann.}$=400 °C (cycle 8), $t_{ann.}$=5 min (cycles 1-7), $t_{ann.}$=30 min (cycle 8)
G (CdO·7ZnO)	Quartz glass (13.4)	8	mixture of precursor I, precursor II and caproic acid in volume proportion of 1:0.022:1.12	0.10 (cycles 1-8)	$v_{heat.}$=15 ˚C/ min (cycles 1–8), $T_{ann.}$=350 °C (cycles 1-7), $T_{ann.}$=400 °C (cycle 8), $t_{ann.}$=5 min (cycles 1-7), $t_{ann.}$=30 min (cycle 8)

*thermal treatment performed by inserting the sample in the preheated chamber

3. RESULTS AND DISCUSSION

XRD patterns of the ZnO and CdO-ZnO thin film are shown in Figs. 1–4.

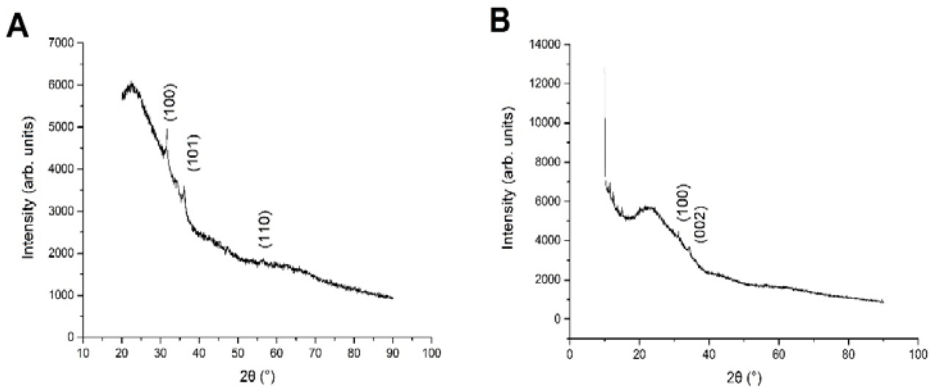

Fig. 1. XRD patterns of films **A** and **B**.

For the ZnO thin film on the glass substrate, several diffraction maxima were observed at (100), (002), (101), (012) and (110) crystallographic plane orientations. For the thin film **B** on the glass substrate, the (100) and (002) crystallographic plane orientations could be observed; however, the diffraction peaks were less intense compared to the diffraction peaks on the ZnO diffractogram.

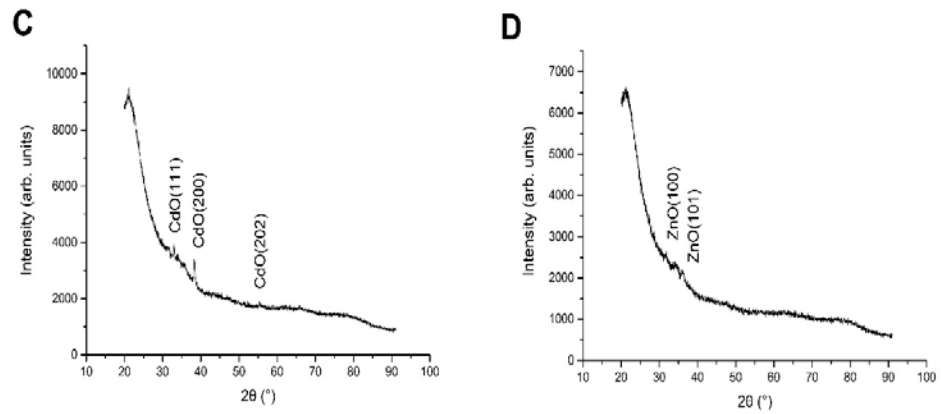

Fig. 2. XRD patterns of films **C** and **D**.

In contrast to the thin film **B** on the glass substrate, on the diffractogram of thin film **C**, which was produced on the quartz glass substrate, additional diffraction maxima at crystallographic plane orientations (111), (200) and (202) could be observed. By comparing the diffraction maxima of all thin films with the data of the Crystallography Open Database [16]–[18], it turned out that all the diffraction maxima (100), (002) and (101) corresponded to the hexagonal wurtzite ZnO struc-

ture. However, the (111), (200) and (202) diffraction maxima corresponded to the cubic CdO structure (creation of mixed ZnO and CdO crystallographic phases was not observed). Taking into account that all diffraction maxima of the thin films were observed at several orientations of crystallographic planes, we concluded that our investigated thin films had polycrystalline structures. Creation of $Cd_xZn_{1-x}O$ crystallographic phase was possible only in case of sample **B** because of shifting of the diffraction peak (100) towards lower angles ($Cd_xZn_{1-x}O$ – solid solution of zinc oxide and cadmium oxide; xCdO·yZnO – a mixture containing several phases, x and y are moles). In case of sample **D**, the shifting of ZnO diffraction peaks was not observed.

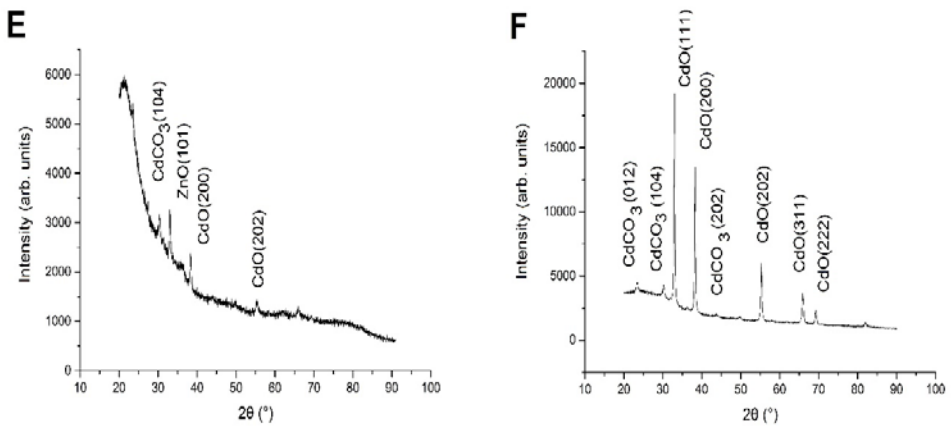

Fig. 3. XRD patterns of films **E** and **F**.

On the diffractograms of samples **E**, **F** and **G** intensive diffraction maxima are visible, which correspond to the otavite $CdCO_3$. The presence of CdO phase with cubic structure in the samples is also confirmed. The presence of mixed $Cd_xZn_{1-x}O$ crystallographic phase is not confirmed by XRD.

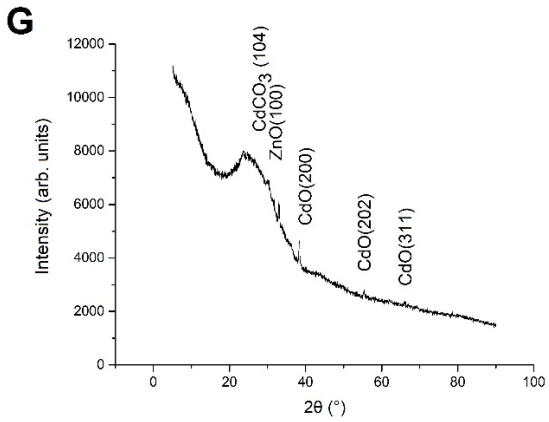

Fig. 4. XRD pattern of film **G**.

In air the second reaction is possible:

$$CdO+CO_2 \xrightarrow{120\text{-}140\ ^\circ C} CdCO_3.$$

The process of the formation of cadmium carbonate after decomposition of organic precursors is also possible, but the process described by the above-mentioned reaction has a higher chance to occur. The process of the decomposition of organic precursors should be performed and investigated in inert atmosphere at higher temperatures. Thin films produced after thermal treatment should be cooled in inert atmosphere to avoid the interaction with carbon dioxide.

The calculated average size of crystallites in the ZnO thin film on the glass substrate is 8–39 nm. For the thin films with chemical composition of CdO·7ZnO, the size of the crystallites of ZnO phase is 15–19 nm and 8–14 nm for the glass and quartz substrates respectively, and the sizes of CdO crystallites are 8–42 nm. It could be observed that the size of the ZnO crystallites diminished in presence of the CdO phase in the sample. The intensities of the diffraction peaks of ZnO phase became also weaker. It is possible that the presence of cadmium affects the formation of ZnO phase with high crystallinity.

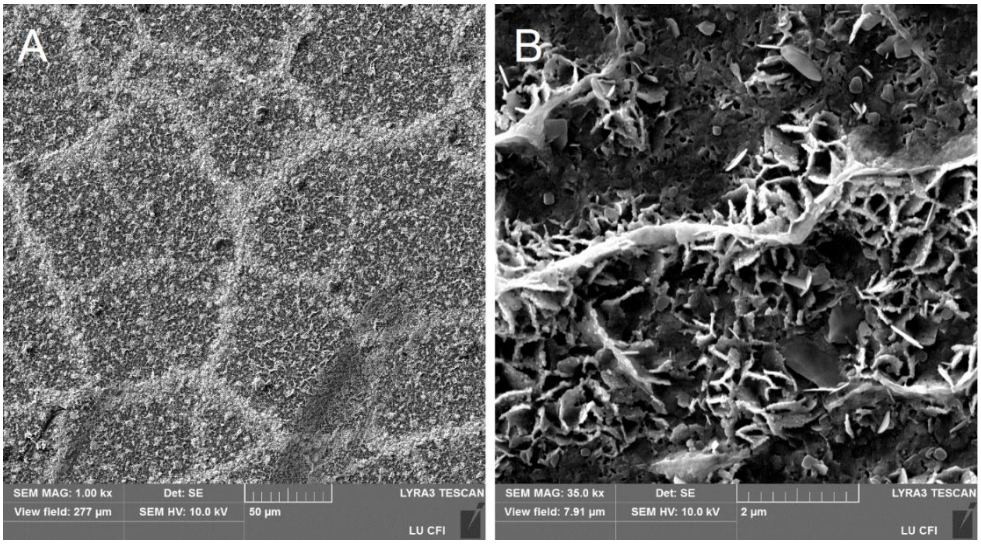

Fig. 5. SEM microphotograph of sample **A** (A – at lower magnification; B – at higher magnification).

The surfaces of the samples **A** and **C** are shown in Fig. 5 and Fig. 6, respectively. The surface of sample **A** has a lower quality and is rougher.

The bad quality of the thin film **A** can be explained by the intensive gas release process when a larger amount of organic precursor is decomposed (see Table 1). The uniform organic layer is not always formed on the substrate after the evaporation of diluent (after thermal treatment non-continuous oxide film is produced); hence, the additional cycle of the application of organic precursor and thermal treatment is necessary to produce a more uniform oxide film. In addition, the temperature of 350 °C may not be sufficient for the total decomposing of organic precursor, so some amorphous phases may remain in the thin film **A**. The results of analysis of SEM

microphotograph are in a good correspondence with the results of profile measurements of the thin films.

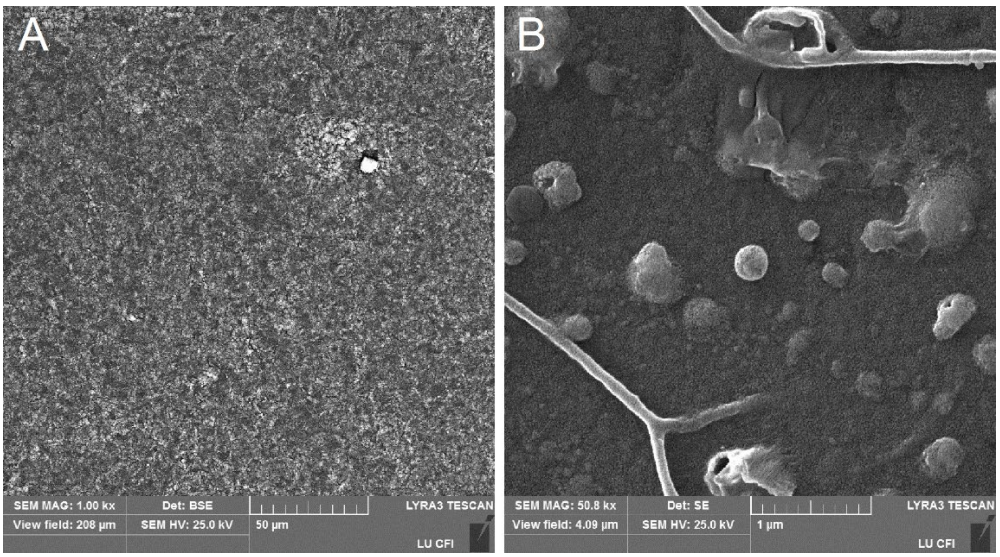

Fig. 6. SEM microphotograph of sample **C** (A – at lower magnification; B – at higher magnification).

Measurements of the thickness of thin films showed that the thin ZnO film on the glass substrate was 150 nm thick, whereas the thickness of the thin films with chemical composition of CdO·7ZnO on both the glass and the quartz glass substrate equalled approximately 100 nm. It was established during the production of thin films that the thickness of the resulting film could be controlled by varying the volume of applied organic solution.

4. CONCLUSIONS

ZnO and CdO-ZnO thin films have been produced for the first time by the extraction-pyrolytic method. The produced CdO and ZnO layers are polycrystalline with an average size of crystallites about 8–42 nm. The formation of the cadmium carbonate phase in the CdO containing films has been confirmed. The resulting quality of thin film depends on its production technology.

ACKNOWLEDGEMENTS

The present research has been supported by the Latvian State Research Programme on Innovative Materials IMIS2 (2014–2017). Technical assistance with SEM measurements provided by Karlis Kundzins at the Institute of Solid State Physics, University of Latvia, is acknowledged. Technical assistance with elemental analysis provided by Linards Skuja at the Institute of Solid State Physics, University of Latvia, is also acknowledged.

REFERENCES

1. Ozgur, U., Alivov, Ya. I., Liu, C., Teke, A., Reshchikov, M. A., Dogan, S., Avrutin, V., Cho, S.-J., and Morkoc, H. (2005). A comprehensive review of ZnO materials and devices. *J. Appl. Phys. 98*, 041301.
2. Ma, D.W., Ye, Z.Z., Lu, H.M., Huang, J.Y., Zhao, B.H., Zhu, L.P., and Zhang, H.J. (2004). Sputtering deposited ternary $Zn_{1-x}Cd_xO$ crystal films on Si(111) substrates. *Thin Solid Films. 461*, 250–255.
3. Wei, M., Boutwell, R.C., Mares, J.W., Scheurer, A., and Schoenfeld, W.V. (2011). Band-gap engineering of sol-gel synthesized amorphous $Zn_{(1-x)}Mg_{(x)}O$ films. *Appl. Phys. Lett. 98*, 261913.
4. Bae, H.S., and Seogil, I. (2004). Ultraviolet detecting properties of ZnO-based thin film transistors. *Thin Solid Films. 469–470*, 75–79.
5. Chou, Sh.M., Teoh, L.G., Lai, W.H., Su, Y.H., and Hon, M.H. (2006). ZnO:Al thin film gas sensor for detection of ethanol vapor. *Sensors*. 6, 1420–1427.
6. Zhao, Zh., Lei, W., Zhang, X., Wang B., and Jiang, H. (2010). ZnO-Based Amperometric Enzyme Biosensors. *Sensors*. *10*, 1216–1231.
7. Chu, Sh., Olmedo, M., Yang, Zh., Kong, J., and Liu, J. (2008). Electrically pumped ultraviolet ZnO diode lasers on Si. *Appl. Phys. Lett. 93*, 181106.
8. Li, K., Li, Y., and Xue, D. (2011). Band gap prediction of alloyed semiconductors. *Funct. Mat. Lett. 4*, 217–219.
9. Coutt, T.J., Perkins, J.D., Ginley, D.S., and Mason, T.O. (1999). Transparent conducting oxides: status and opportunities in basic research. In *195th Meeting of the Electrochemical Society*, 2–6 May 1999. Seattle, Washington.
10. Lee, J.H., and Park, B.O. (2003). Transparent conducting ZnO:Al, In and Sn, thin films deposited by the sol-gel method. *Thin Solid Films*. *426*, 94–99.
11. Hiramatsu, M., Imaeda, K., Horio, N., and Nawata, M. (1998). Transparent conducting ZnO thin films prepared by XeCl excimer laser ablation. *J. Vac. Sci. Technol. A*. *16*, 669–673.
12. Lee, J., Li, Z., Hodgson, M., Metson, J., Asadov, A., and Gao, W. (2004). Structural, electrical and transparent properties of ZnO thin films prepared by magnetron sputtering. *Curr. Appl. Phys. 4* (2-4), 398–401.
13. Konstantinidis, S., Hemberg, A., Dauchot, J.P., and Hecq, M. (2007). Deposition of zinc oxide layers by high-power impulse magnetron sputtering. *J. Vac. Sci. Technol. B*. *25*, 19–21.
14. Fan, J.C., Sreekanth, K.M., Xie, Z., Chang, S.L., and Rao, K.V. (2013). p-Type ZnO materials: Theory, growth, properties and devices *Pro. Mater. Sci. 58*, 874–985.
15. Khol'kin, A.I., and Patrusheva, T.N. (2006). *Extraction-Pyrolytic Method: Production of Functional Oxide Materials*, Moscow: KomKniga.
16. Grazulis, S., Daskevic, A., Chateiger, D., Lutterotti, L., Quios, M., Serebryanaya, N. R., Mock, P., Downs, R. T., and Le Bail, A. (2012). Crystallography Open Database (COD): an open-access collection of crystal structures and platform for world-wide collaboration. *Nuc. Acids Res. 40*, 420–427.
17. Grazulis, S., Chateigner, D., Downs, R. T., Yokochi, A. T., Quiros, M., Lutterotti, L., Manakova, E., Butkus, J., Moeck, P., and Le Bail, A. (2009). Crystallography Open Database – An open-access collection of crystal structures. *J. Appl. Cryst. 42*, 726–729.
18. Downs, R. T., and Hall-Wallace, M. (2003). The American Mineralogist Crystal Structure Database. *Am. Mineral. 88*, 247–250.

ZnO UN CdO-ZnO PLĀNO KĀRTIŅU IEGŪŠANA AR EKSTRAKCIJAS-PIROLĪTISKO METODI

A. Cvetkovs, O. Kiseļova, U. Rogulis, V. Serga, R. Ignatāns

K o p s a v i l k u m s

Darbā ZnO in CdO-ZnO plāno kārtiņu iegūšanai uz stikla un kvarca stikla pamatnēm tika izmantota ekstrakcijas-pirolītiskā metode. Rentgenstaru difrakcijas dati norāda uz ZnO un CdO kristālisko fāžu veidošanos ar vidējo kristalītu izmēru 8-42 nm kārtiņās. Ar profilometru noteiktais iegūto kārtiņu biezums sasniedza 150 nm. Virsmas morfoloģijas mērījumi parāda, ka kārtiņas var būt nelīdzenas un var pilnīgi nepārklāt pamatnes virsmu. Mainot kārtiņu iegūšanas tehnoloģiju, var būtiski ietekmēt pārklājumu kvalitāti. Par to liecina iegūtās kārtiņu SEM mikrofotogrāfijas.

02.11.2015.

LATVIAN JOURNAL OF PHYSICS AND TECHNICAL SCIENCES
2016, N 3

DOI: 10.1515/lpts-2016-0022

ENVIRONMENTAL MONITORING

IMPACT OF THE FORMER SALASPILS NUCLEAR REACTOR ON THE SURROUNDING TERRITORY

D. Riekstina[1], J. Berzins[1], T. Krasta[1], G. Kizane[2], J. Rudzitis[2]
[1]Institute of Solid State Physics, University of Latvia,
8 Kengaraga Str., Riga, LV-1063, LATVIA
[2]Institute of Chemical Physics, University of Latvia,
19 Raina Blvd., Riga, LV-1586, LATVIA

The paper presents results of the long-term environment radioactivity monitoring in the vicinity of the decommissioned Salaspils Nuclear Reactor. Data include Cs-137 contamination levels of soils, H-3 concentration in ground waters, as well as gross beta activity of sewage and rainwater drainage of SNR. Special attention is devoted to the radioactive pollution of water due to leakage from the special wastewater basin detected in December 2014.

Keywords: *artificial radionuclides: Cs-137, H-3, beta-activity, environment radioactivity monitoring, nuclear reactor.*

1. INTRODUCTION

Radiation hazard for population is a topic attracting nowadays growing attention. According to public opinion, nuclear reactors are regarded as the most dangerous potential sources of such hazards. The Salaspils Nuclear Reactor (SNR) near Riga had been in operation for a long period (1961–1998) which could have resulted in pollution of the closest surrounding territory with artificial radionuclides: products of activation or fission. The most important of these artificial radionuclides are Cs-137, and H-3.

The use of beryllium (Be) cassette for neutron reflection in the reactor core resulted in the production of tritium in water of the reactor tank, and first contour. Nuclear reactions involved in the tritium production process (Eq.1) include fast neutron capture by ^{9}Be nuclei, and thermal neutron capture by ^{6}Li and ^{3}He nuclei, as well as beta-decay of ^{6}He, and ^{3}H [1].

$$\begin{aligned} &{}^{9}\mathrm{Be} + \mathrm{n}\ (1\text{-}10\ \mathrm{MeV}) \rightarrow {}^{10}\mathrm{Be}^{*} \rightarrow {}^{4}\mathrm{He} + {}^{6}\mathrm{He} - 0.64\ \mathrm{MeV}; \\ &\qquad\qquad\qquad\qquad\qquad\qquad\qquad\qquad \downarrow 0.8\ \mathrm{s} \\ &\qquad\qquad\qquad\qquad\qquad\qquad\qquad\qquad {}^{6}\mathrm{Li} + \beta^{-} \\ &{}^{6}\mathrm{Li} + \mathrm{n}\ (\mathrm{th}) \rightarrow {}^{3}\mathrm{H} + {}^{4}\mathrm{He} + 4.7\ \mathrm{MeV}; \\ &\qquad\qquad \downarrow 12.3\ \mathrm{yr} \end{aligned} \qquad (1)$$

$$^{3}He + \beta^{-}$$
$$^{3}He + n\ (th) \rightarrow {}^{3}H + p^{-}.$$

Tritium could have leaked into environment (in the form of vapour and contaminated water).

The regular Cs-137 monitoring of soils around the decommissioned SNR has been carried out since 1998. Activity monitoring of gamma- and beta-ray emitting radionuclides in the ground waters around SNR was started in 1990. Tritium monitoring of ground waters has been carried out since 1997. Some results have been published earlier in [2], [3].

The aim of present research is to provide an overview of the long-term study of presence and concentration of artificial radionuclides in soils and waters of the three kilometre radius area around SNR after its shutdown. Data include Cs-137 activity in soils, tritium and gross beta activity in ground waters and sewage. Accumulation and migration of artificial radionuclides in the soil and ground waters of SNR vicinity have been studied as well. The obtained results are compared with the background radioactivity level in the rest of Latvian territory [4], [5], as well as with national and EU regulation requirements [6], [7].

In December 2014, a high activity concentration (~ $5 \cdot 10^3$ Bq/l) of tritium was discovered in the control wells near the special sewage water storage basins. The cause of this incident was water leakage due to basin's metal wall corrosion. Systematic radionuclide contamination control of water was carried out during all stages of deactivation and repair works. The present paper provides an overview of these measurements as well as takes stock of situation after the liquidation of this pollution source.

2. EXPERIMENTAL PROCEDURE

For the regular monitoring of Cs-137 activity in soils of the three kilometre zone around SNR, five fixed checkpoints were selected (3 points inside, and 2 points outside the SNR territory). Each sampling point had an area of 1 m^2. Every year in August–September, 5 samples (sample size – 8 cm x 8 cm) were taken at each checkpoint from the upper soil layer (0–5 cm) and mixed. Then, samples were dried at 105 °C to attain constant weight, homogenized, filled into 1 l Marinelli beakers and weighted. Radionuclide concentration measurements were performed using the gamma-ray spectrometry methods [8], [9] employing the high resolution HPGe gamma-ray spectrometers Ortec or Canberra with the Genie™ 2000 software system [10]. Massic activity of Cs-137 in soil samples was determined from intensity of the 661.657 keV γ-line. The uncertainty of measurement results was within the range of 3–10 %, the minimal detectable activity (MDA) – 0.3 Bq/kg.

Gamma-ray spectrometers were calibrated for gamma-ray energy and efficiency measurements using certified mixed standard volume source traceable to NIST. Regular energy and efficiency stability checks of gamma-ray spectrometers were carried out using certified Co-60, Cs-137, and K-40 sources.

In order to monitor tritium concentration in the ground waters around SNR,

control wells were made at distances ca. 5 to 200 m from the reactor tank and special sewage basins (see Fig. 1). Ten wells are located inside SNR territory, and twelve wells – outside the reactor fence. The control wells are numbered and grouped as A, B, and V according to their depth as follows (see Fig. 2). The distance between A, B, and V wells within groups 1–4 is 1.2 m; between wells 7A and 7V − 0.75 m; and between wells 8A and 8V − 0.7 m. The well X1 is 4 m, and the well X2 – 6 m deep.

The liquid scintillation counting method [11] was used for determination of tritium activity in ground waters. Collected samples of ground water were distilled and then mixed with a scintillation cocktail (OptiPhase "HiSafe"3) in a polyethylene vial. The optimal mixing ratio was 8 ml of distillate, and 12 ml of scintillation cocktail. Measurements of tritium activities were performed with the liquid scintillation spectrometer (Packard TRI-CARB 2100 or Hidex 300 SL). Measurement time was up to 12 hours or until statistical uncertainty less than 2 % was achieved. For this counting time, MDA was 4 Bq/l.

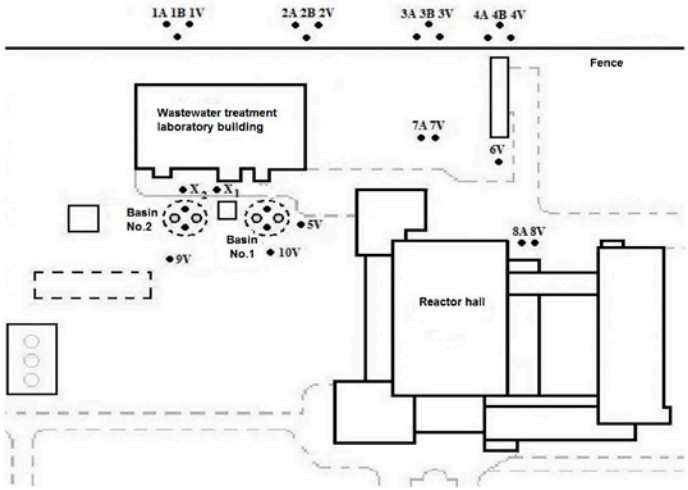

Fig. 1. Location of control wells in the territory of SNR.

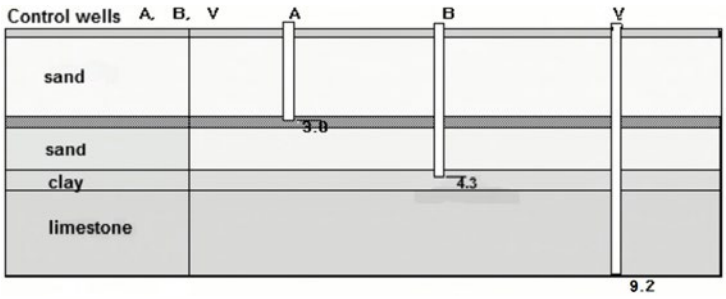

Fig. 2. Depth distribution of control wells.

For determination of gross beta-activities [12], collected 1 l samples of ground water and/or sewage were evaporated. Measurements were performed using the calibrated Tennelec-Solo device.

Credibility of obtained results was ensured by the quality assurance and control according to the main requirements of the ISO/IEC 17025:2008 standard [13].

3. RESULTS AND DISCUSSION

3.1 Monitoring of Soils in the SNR Territory

Measurements of radioactivity in the soil samples of the three kilometre zone around SNR established only presence of Cs-137, as well as natural radionuclides: K-40, and decay products of Th-232 and U-238 chains [2]. It was found that concentration of Cs-137 differed significantly in the adjacent places. These variations could be explained by different sorption of Cs-137 in various soil types [14] and location of the checkpoint (grassland, plough land, coniferous or leafy forest, etc.). The massic activity of Cs-137 in the grassland and plough land was from 0.3 up to 26 Bq/kg. In forest, the massic activity of Cs-137 was from 38 to 227 Bq/kg. The maximal Cs-137 massic activity in the SNR territory – 227 Bq/kg – was found in the pine forest.

Let us compare these results with Cs-137 activity from the global fallout including Chernobyl. The average Cs-137 massic activity in the Latvian soil was determined at 140 Bq/kg [5]. In the east part of Latvia, the maximal Cs-137 massic activity was determined at 319 Bq/kg, while in the west regions – between 150 and 950 Bq/kg [4]. Therefore, the Cs-137 activity level in the SNR territory is below the contamination values established in Latvian soils [5], [15].

Figure 3 presents the minimal and maximal massic activity of Cs-137 in the vicinity of SNR for each year starting with 2003. The observed variations of Cs-137 massic activity depend on the soil material (clay, sand, or peat), and the location of sampling point (forest or grassland).

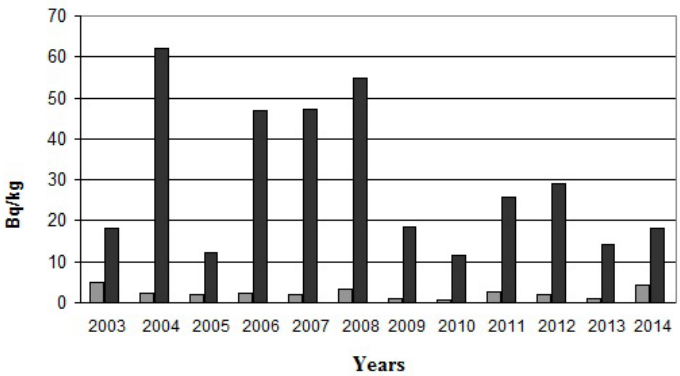

Fig. 3. Minimal and maximal annual massic activity of Cs-137 in the soils of SNR territory.

3.2 Monitoring of Ground and Sewage Waters

Figure 4 presents the results of tritium monitoring of ground waters in two control wells. The well 2B (see Figs. 1, and 2) is 4.3 m deep in the clay level and located on the ground water stream outside the reactor's fence. The well 10V is

9.2 m deep in the limestone level close to the SNR wastewater basin No. 1. The distance between wells 2B and 10V is ~50 m. We compare data for ground water samples taken in October of each year. The established seasonal variations of tritium concentration related to the amount of precipitations are within 20 % limits. The increased tritium concentration in the well 10V in the period of 2003–2004 can be explained by the washing out of tritium from the gypsum caverns (within the SNR territory) due to meteorological conditions.

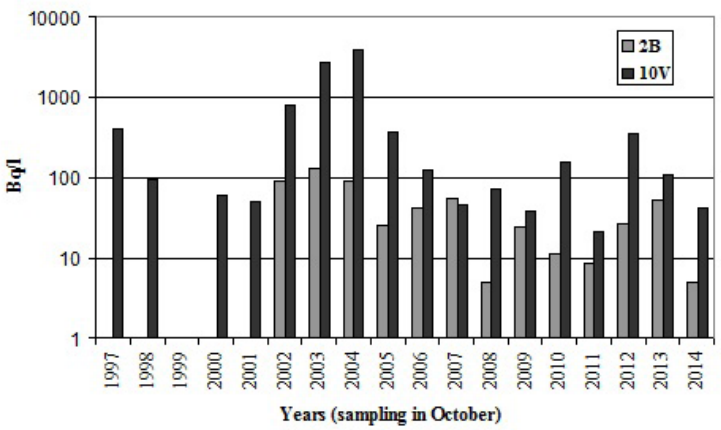

Fig. 4. Tritium concentration in wells 2B and 10V.

Waters of the SNR territory were also monitored for the gross beta activity. In the ground waters, this activity varied in the range from 0.05 to 0.35 Bq/l. The allowed gross beta activity level for water is 1 Bq/l [6]. The gross beta activity of water from the SNR sewage and rainwater drainage systems (Fig. 5) displayed correlation with reactor operation (1994–1998) and the partial dismantling of reactor systems (2007–2009). In 1998, the gross beta activity was smaller because SNR operation stopped in June.

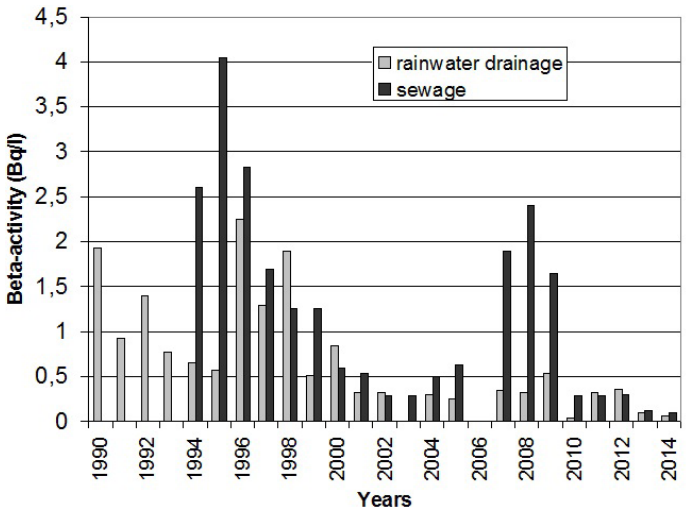

Fig. 5. Average annual beta activity of water in the sewage and drainage of SNR.

3.3. Radioactive Pollution Incident at the Decommissioned SNR

In December 2014, a high level of water pollution with tritium was detected in the control wells X1, and X2 (see Fig. 1): $4.96 \cdot 10^3$, and $2.15 \cdot 10^3$ Bq/l, respectively. The supposed cause was leakage from special sewage underground basin No.1 due to metal corrosion. Special sewage basins No.1 and No.2 are welded stainless steel tanks (diameter – 624 cm; height – 230 cm; metal thickness – 4 mm) enclosed within concrete housings. Basins were built in 1960.

In order to liquidate the possible environmental pollution source and to eliminate possibility of future incidents, the deactivation and repair works plan was elaborated. This plan included regular dosimetry and water radioactivity control measurements and was approved by the National Radiation Safety Authority.

101.2 m^3 of contaminated water from sewage basins No.1, and No.2 were pumped out and filled into double layer containers (a 100 litre plastic barrel within a 200 litre metal barrel). Maximal measured dose rate on the outer surface of water containers was 0.9 – 1.0 μSv/h due to the total Cs-137 activity of water in the container. These containers were stored: part in the temporary storage building, and part in the former reactor hall.

The radioactive sludge mixed with the ion exchange resin covering bottom of basin No.1 was gathered, packed in 14 metal barrels (2800 litres) and stored within A-172 type containers in the reactor hall. Since dose rate on some filled barrels was 25-30 μSv/h, three barrels with sludge and scrap metal parts were cemented within A-172 type containers.

When all contaminated water and sludge were removed, both sewage basins were washed with pressurized water streams. Resulting radioactive water (~150 liters) was pumped into the above-mentioned double layer containers and stored.

After the decontamination, the ambient gamma dose rate in basin No.1 was 1.5–3.0 μSv/h, and in basin No. 2 – 0.3–0.55 μSv/h.

Then, the seams of metal tanks in sewage basins No. 1, and No. 2 were checked and all detected cracks were welded.

Radioactivity control measurements were carried out during all stages of the emergency works as well as after completion of the task. Table 1 presents Cs-137, and H-3 activity levels in both basins at main stages of the work. Registered activity of Co-60, natural radionuclides K-40, and U-238 was negligible, except in sludge at the bottom of basin No.1 where Co-60 massic activity reached 4330 Bq/kg.

Table 2 presents maximal Cs-137 and H-3 activities detected in the water of control wells of the SNR territory. Maximal activities were found in wells X1 and X2, which were closest to the basins. Figure 6 presents variations of tritium activity in control wells X1 and X2 during the incident and emergency works. The maximal Cs-137 massic activity 12.9 Bq/kg was detected in the well X2 in the middle of March, 2015 when basins were washed.

Radionuclide content in other control wells of the SNR territory (see Fig. 7) was much lower: the maximal activity level ~600 Bq/l was observed in the well 5V. In some control wells, presence of natural radionuclides K-40 and U-238 in water was detected as well. It could be explained by washing out of clay layer.

Table 1

The Radioactivity Control Data of Sewage Basins During the Incident

Date	Basin No.1		Basin No.2		Comment
	Cs-137 Bq/kg	H-3 Bq/l	Cs-137 Bq/kg	H-3 Bq/l	
01.12.2014	477 ± 4 %	$3.23 \cdot 10^5$ ± 8 %	513 ± 4 %	$1.59 \cdot 10^5$ ± 8 %	Water before the incident
06.02.2015			46 ± 4 %	$1.3 \cdot 10^3$ ± 8 %	Water removed from basin No.2
10.03.2015	471 ± 4 %	$2.44 \cdot 10^5$ ± 8 %			Water removed from basin No.1
10.03.2015	$3.8 \cdot 10^5$ ± 4 %	-	-	-	Sludge
14.05.2015	5.2 ± 5 %	-	8 ± 4 %	-	Control measurements

Table 2

Maximal Cs-137 and H-3 Activity Levels Detected in the Water of Control Wells of the SNR Territory During the Incident

Well No.	Cs-137 Bq/kg	H-3 Bq/l
X1	2.8 ± 5 %	$3.88 \cdot 10^4$ ± 8 %
X2	12.9 ± 4 %	$9.53 \cdot 10^4$ ± 8 %
5V	1.7 ± 5 %	581 ± 9 %
9V	3.6 ± 5 %	69 ± 21 %
10V	1.6 ± 5 %	193 ± 12 %
7A	< 0.5	7 ± 35 %
1B	1.2 ± 6 %	50 ± 27 %
2A	9 ± 4 %	71 ± 21 %
2B	1.4 ± 5 %	7 ± 35 %
4A	<0.5	< 4
4B	<0.5	< 4

Measurements carried out after the incident showed that tritium content in wells outside the reactor fence was below limits allowed for drinking water.

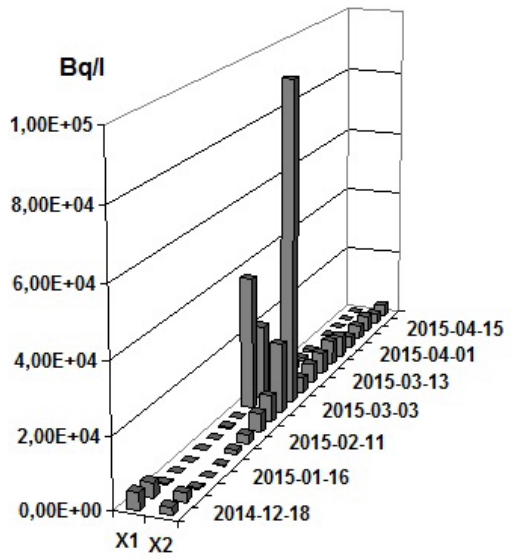

Fig. 6. Tritium activity concentration of water in control wells X1 and X2 during the incident.

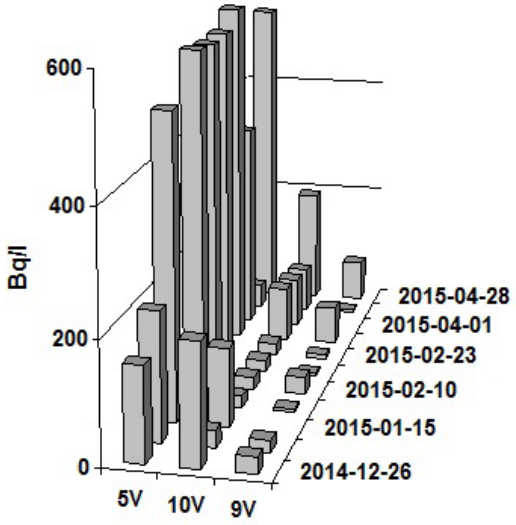

Fig. 7. Tritium activity concentration of water in other control wells close to the basins.

4. CONCLUSIONS

The obtained results presented dynamics of artificial radionuclide concentration in soils and ground waters in the vicinity of SNR depending on years and location.

1. The results of Cs-137 monitoring in soils showed that the massic activity varied in different places of the SNR territory. However, it did not exceed the average global Cs-137 fallout level value in the Latvian territory (~140 Bq/kg).

2. The results of tritium, activity measurements show variation within a wide range (5–8000 Bq/l) for particular years. Seasonal changes of activity were established as well. The activity concentration of tritium in the wells outside the SNR territory was below the level permitted for drinking water in Latvia (100 Bq/l).
3. The determined gross beta activity level in the ground waters of the SNR territory was below 0.35 Bq/l, which was within limits permitted by regulations.
4. The performed monitoring allowed timely establishing the emergency situation related to the water leakage from the storage basin and ensuring the elimination of the possible large scale environmental pollution.
5. The monitoring showed that the amount of radionuclides produced by SNR had little impact on the total radionuclide content in the Latvian environment.

REFERENCES

1. Turner, J.E. (2007). *Atoms, Radiation, and Radiation Protection*. Weinheim: WILEY-VCH Verlag GmbH & Co. KGaA.
2. Berzins, J., Riekstina, D., Veveris, O., and Malnacs, J. (2009). Radiation control of some contaminated territory of Latvia. In *Leben mit Stralung – von den Grundlagen zur Praxis. 6*. Gemeinsame Tagung der Österreichischen Verbundes für Strahlenschutz ÖVS und der Deutsch/Schweizerischen Fachverbandes für Strahlenschutz FS mit Workshop der Österreichishen Gessellschaft für Medizinishe Physik ÖGMP. 41. Jahrestagung der FS. 21–25 September 2009, Alpbach, Tirol (pp. 182–187). TÜV Media GmbH, TÜV Rheinland Group, Köln.
3. Riekstina, D., and Veveris, O. (2010). Tritium concentration in drinking and ground water in Latvia. In *International Conference on Advances in Liquid Scintillation Spectrometry*. 6–10 September 2010, Paris, France (pp. 95–98) Joe Christensen, Inc., Lincoln, Nebraska, USA.
4. Veveris, O., Riekstina, D., Taure, I., and Skujina, A. (2003). Forest ecosystem as accumulator of radionuclides. *Ecology 2*, 53–55.
5. Rissanen, K., Ylipieti, J., Salminen, R., That, K., Giliucis, A., and Gregorauskiene, V. (2005). Cs-137 concentrations in the uppermost humus layer in the Baltic countries in 2003. *INIS 36(47),* Ref.No. 36109090. IAEA.
6. Latvian Cabinet of Ministers. (2002). *Regulation of Protection against Ionizing Radiation.* Regulations No.149, adopted 09.04.2002 with amendments No.629 of 04.11.2003. Riga.
7. European Commission. (1998). *Directive 98/83/EC of 3 November 1998 on the Quality of Water Intended for Human Consumption.* Luxembourg.
8. Latvian State Standard. (2008). *LVS ISO 10703:2008 Water Quality – Determination of the Activity Concentration of Radionuclides – Method by High Resolution Gamma-Ray Spectrometry.* Riga
9. Latvian State Standard. (2000). *LVS ISO 257:2000 Building Material Quality – Determination of Radionuclides and Specific Activity of Radionuclides in Building Materials by Gamma Spectrometry.* Riga.

10. Canberra Industries. (1997). *GENIE-2000. Basic Spectroscopy (Standalone) VI.2A Copyright.*
11. Latvian State Standard. (2011). *LVS ISO 9698:2011 Water Quality – Determination of Tritium Activity Concentration – Liquid Scintillation Counting Method.* Riga.
12. Latvian State Standard. (2009). *LVS ISO 10704:2009 Water Quality – Measurement of Gross Alpha and Gross Beta Activity in Non-saline Water. The Source Deposit Method.* Riga.
13. International Organization for Standardization. (2008). *ISO/IEC 17025:2005 General Requirements for the Competence of Testing and Calibration Laboratories.*
14. Stauton, S., and Raunband, M. (1997). Adsorption of Cs-137 on montmorillonite and illite: Effect of charge compensating cation, ionic strength, concentration of Cs, K and fulfic acid. *Clay and Clay Minerals 45(2)*, 251–260.
15. Riekstina, D., Veveris, O., and Zalitis, P. (1997). Forest litter as indicator of radioactive pollution. *Baltic Forestry 3*, 35–40.

APKĀRTĒJĀS VIDES MONITORINGA REZULTĀTI BIJUŠĀ SALASPILS KODOLREAKTORA TERITORIJĀ

D. Riekstiņa, J. Bērziņš, T. Krasta, G. Ķizāne, J. Rudzītis

Kopsavilkums

Darbs prezentē ilgākā laika periodā veiktā vides monitoringa rezultātus bijušā Salaspils pētnieciskā reaktora teritorijā. Ir sniegti dati par Cs-137 koncentrāciju augsnē, kā arī tritija koncentrāciju gruntsūdeņos. Tāpat sniegti dati par summāro beta aktivitāti gruntsūdeņos speciālās un lietus kanalizācijas ūdeņos. Īpaša uzmanība pievērsta radionuklidu koncentrācijas mērījumiem 2014. gada decembrī notikušās radioaktīvo ūdeņu noplūdes laikā, avārijas situācijas likvidācijas laikā, kā arī stāvokļa novērtēšanai pēc incidenta.

17.12.2015.